Fifty-Year Trends in Global Ocean Salinities and Their Relationship to Broad-Scale Warming

PAUL J. DURACK

Centre for Australian Weather and Climate Research, CSIRO Marine and Atmospheric Research, and Institute for Marine and Antarctic Studies, University of Tasmania, and Wealth from Oceans National Research Flagship, CSIRO, Hobart, Tasmania, Australia

SUSAN E. WIJFFELS

Centre for Australian Weather and Climate Research, CSIRO Marine and Atmospheric Research, and Wealth from Oceans National Research Flagship, CSIRO, Hobart, Tasmania, Australia

(Manuscript received 10 August 2009, in final form 18 March 2010)

ABSTRACT

Using over 1.6 million profiles of salinity, potential temperature, and neutral density from historical archives and the international Argo Program, this study develops the three-dimensional field of multidecadal linear change for ocean-state properties. The period of analysis extends from 1950 to 2008, taking care to minimize the aliasing associated with the seasonal and major global El Niño–Southern Oscillation modes. Large, robust, and spatially coherent multidecadal linear trends in salinity to 2000-dbar depth are found. Salinity increases at the sea surface are found in evaporation-dominated regions and freshening in precipitation-dominated regions, with the spatial pattern of change strongly resembling that of the mean salinity field, consistent with an amplification of the global hydrological cycle. Subsurface salinity changes on pressure surfaces are attributable to both isopycnal heave and real water-mass modification of the temperature–salinity relationship. Subduction and circulation by the ocean's mean flow of surface salinity and temperature anomalies appear to account for most regional subsurface salinity changes on isopycnals. Broad-scale surface warming and the associated poleward migration of isopycnal outcrops drive a clear and repeating pattern of subsurface isopycnal salinity change in each independent ocean basin. Qualitatively, the observed global multidecadal salinity changes are thus consonant with both broad-scale surface warming and the amplification of the global hydrological cycle.

1. Introduction

Changes to the global hydrological cycle are anticipated as a consequence of anthropogenic climate change (Solomon et al. 2007; Held and Soden 2006). Climate projections feature an enhancement of the hydrological cycle as the troposphere warms and thus increases its ability to store and transport water vapor (Bindoff et al. 2007; Emori and Brown 2005; Meehl et al. 2007; Trenberth et al. 2007). Measurements of the water flux between the atmosphere and the ocean/land surface over the past 50 yr are, however, inadequate for assessing past global change. Precipitation records express noisy, high-frequency variations spatially and temporally and are only measured adequately on land in a few highly populated regions. Flux measurements over the oceans are even more limited by their extreme scarcity and the poor quality of historical marine meteorological ship reports from vast remote regions of the global oceans.

The oceans compose 71% of the earth's surface area and 97% of the global water inventory, with 80% of the surface water flux occurring over the oceans (Schmitt 1995). The global ocean's salinity field reflects the large-scale long-term balance between the surface freshwater flux [evaporation minus precipitation (EP) and terrestrial runoff minus the total surface freshwater flux (F_W)] and the ocean's advective and mixing processes. Any change in the hydrological cycle, therefore, will be reflected in the ocean salinity field. Large and coherent multidecadal changes in the ocean's salinity field have already been reported on global and regional scales.

Corresponding author address: Paul J. Durack, CSIRO Marine and Atmospheric Research, GPO Box 1538 Hobart, TAS 7001, Australia.
E-mail: paul.durack@csiro.au

DOI: 10.1175/2010JCLI3377.1

Antonov et al. (2002) and Boyer et al. (2005) reported global salinity changes on pressure surfaces, showing that surface subtropical waters are generally becoming saltier and high-latitude waters are freshening. These results were based on a linear least squares fit to objectively analyzed global (5 yr) anomaly fields for the period 1948–96 (Antonov et al. 2002) and 1957–96 (Boyer et al. 2005). However, a large unresolved variance in Boyer et al. (2005) for many regions of key salinity trend signals indicated a highly noisy result for their linear fit. Antonov et al. (2002) found similar spatial patterns of salinity changes but with smaller magnitudes.

Curry et al. (2003) compared the time periods 1955–69 and 1985–99 and examined salinity changes for the entire Atlantic basin on both pressure and density surfaces. Similar to Boyer et al. (2005), they found increased salinity in the subtropical evaporation-dominated regions between 25°S and 35°N but with larger magnitudes. Additionally, the higher-latitude South Atlantic ventilated thermocline waters freshened, as did the underlying Antarctic Intermediate Water (AAIW) and Upper Circumpolar Deep Water (UCDW) but with smaller magnitudes.

Six transoceanic hydrographic sections were analyzed by Wong et al. (1999), comparing historical data (1962–1970) to the late 1980s and early 1990s in the North and South Pacific and south Indian Oceans. Using a snapshot approach (similar to Curry et al. 2003), they discovered coherent and broad-scale freshening in North Pacific Intermediate Waters (NPIW) and a weaker freshening in the AAIW in the south Indian Basin.

A recent study by Cravatte et al. (2009) uncovered large changes to ocean properties in the tropical western Pacific warm pool, using data for the 1955–2003 period derived from a collection of different sampling methods. They concluded that a large broad-scale freshening and density decrease had occurred and that the warm-water volume and horizontal extension of the warm pool had also increased markedly over this period.

A large decadal variability is present in the observed historical salinity record. Dickson et al. (1988) described ''the great salinity anomaly'' in the North Atlantic, where salinity anomalies of −0.15 advected around the basin from the late 1960s through to the early 1980s. Grodsky et al. (2006) analyzed a 40-yr time series in the equatorial Atlantic, observing a surface salinity increase from 1965 to 1985 of around +0.15, with a similar magnitude reduction from 1995 to 2005. This highlights the potential for aliasing of decadal variability into a multidecadal difference when comparing snapshots. For example, along the 32°S trans-Indian section, Bryden et al. (2003) found that thermocline waters freshened from 1965 to 1987 and then became saltier after 1987. Additionally, the seasonal cycle and interannual variability can also represent a source of aliasing between snapshots. This issue is particularly relevant in the data-sparse Southern Hemisphere, where historical data largely exists for the austral summer only.

Although salinity changes at the ocean surface are predominantly driven by F_W changes, ocean circulation shifts may also play a role and, consequently, understanding subsurface salinity changes becomes complex. Adiabatic vertical shifts (or heave) of density surfaces driven by wind changes will cause salinity change on a pressure surface without any real change to the ocean freshwater inventory or water masses. To avoid confusing this heave effect with water-mass modification, analyses of salinity changes are often carried out along a neutral density (hereafter density) surface or isopycnal. Bindoff and McDougall (1994) have attempted to provide a framework for attributing salinity changes on isopycnals due to ''pure warming,'' ''pure freshening,'' or ''pure heave.'' However, this framework does not take into account horizontal shifts in isopycnals, which may be driven by surface heat and freshwater fluxes or circulation changes.

This study presents global multidecadal linear trends of ocean salinity, both in a density and pressure framework, for the period 1950–2008. Aliasing of the salinity change signal has been minimized by explicitly resolving the global and regional detail of the ocean's mean spatial, seasonal, El Niño–Southern Oscillation (ENSO) responses, and the 50-yr linear trend simultaneously. The enhanced methodology improves on the results obtained by previous works (e.g., Antonov et al. 2002; Bindoff and McDougall 2000; Boyer et al. 2005; Cravatte et al. 2009; Curry et al. 2003; Grodsky et al. 2006; Helm 2008; Hosoda et al. 2009; Roemmich and Gilson 2009; Wong et al. 1999, 2001—a detailed comparison is included in Table 1). In addition, this novel analysis exploits the unprecedented spatial and seasonal coverage of the data provided by the international Argo Program (Gould et al. 2004), combining it with quality-controlled historical data.

2. Data sources and quality control

Over 1.6 million vertical profiles of salinity (PSS-78), potential temperature, and approximate neutral density γ^a (in units of kg m^{-3} minus 1000; McDougall 1987; McDougall and Jackett 2005) were assembled, sourced from the Selected Hydrographic Dataset (SeHyD; Kobayashi and Suga 2006), the Indian Ocean Hydrobase (IOHB; Kobayashi and Minato 2005), Hydrobase2 (Curry 2002), and the Southern Ocean Database (SODB; Orsi and Whitworth 2010). These historical datasets (Table 2) were augmented with the April 2009 version of the profile

data from the Argo Program (both real time and delayed mode; Gould et al. 2004). Argo floats with known sensor errors, as outlined on the Argo team Web site (available online at http://www.argo.net), were excluded from the analysis.

Duplicate profiles were removed by finding matches in time and location using tolerances of 1 day and 0.02° in both latitude and longitude (Table 2). A gross-range check of the remaining data was then undertaken with valid data required to satisfy a salinity range of 20–42, in situ temperature of −2.3°–35°C, and pressure from 0 to 10 000 dbar. This range check was particularly useful for the real-time Argo data, which has not undergone expert quality control.

All profiles were then linearly interpolated onto both uniform pressure (0–5500 dbar) and density (21–28 kg m^{-3}) grids. For the pressure analysis, profile salinity and temperature values were assumed constant above 30 dbar if a shallower reading was absent. This then led to almost complete profile coverage at the surface, dropping to 57% at 500 dbar, 12% at 2000 dbar, and just 4% coverage at 2500 dbar.

3. Local parametric fit

The method described by Ridgway et al. (2002) and Alory et al. (2007) was adapted for this analysis, where a spatial and temporal parametric model was fitted to data located within a search ellipse for a target location. The fit was then consecutively undertaken across a fixed latitude and longitude grid for parameters on either a pressure or density surface.

For each target location, data were collected within a spatial ellipse with a latitude (zonal) radius twice that of longitude. The search radius was expanded until a minimum of 1000 observations were found and each decadal bin (from 1950 to 2008) contained a minimum of 10 data points. Consequently, the spatial footprint of the data fit for each point was dependent on the availability of observations both spatially and historically, and so resolved scales were small where historical data coverage was good (Northern Hemisphere basins, in particular the Atlantic) and large where historical coverage was poor (the central South Pacific and interior Indian Ocean). A maximum radius of 1100 km was set, resulting in a small analysis ''hole'' of around 10° in longitude and latitude, centered at 35°S, 142°W in the central South Pacific, where historical coverage is very sparse. Linear interpolation on pressure and density surfaces across this hole allowed a complete global analysis to be formed.

Data from marginal seas were excluded—the Mediterranean Sea, Baltic Sea, Red Sea, Persian Gulf, Indonesian Archipelago (China Seas, Sea of Japan, Java Sea, Banda Sea, and Arafura Sea), Okhotsk Sea, and Hudson Bay (Fig. 1a). Data were also labeled by basin so that only the target location's profiles were included during the fit, which prevented the inclusion of Atlantic (or Pacific) data into a Pacific (or Atlantic) local fit, such as would occur near the narrow Isthmus of Panama for example (Fig. 1b). To ensure continuity of source data in the Southern Ocean, basin masking was disabled south of 55°S in the Pacific, 34°S in the Atlantic, and 42°S in the Indian Ocean Basins (Fig. 1a).

The 1000 or more proximate observations were normalized and data exceeding 5 standard deviations or more from the sample mean were removed. For each variable V a multiparametric regression in space and time around the target coordinate (x_0, y_0) was undertaken with the following form:

$$
\begin{aligned}
V_{(x,y,t)} = {} & S_1 + S_2 x + S_3 x^2 + S_4 y + S_5 y^2 + S_6 xy + A_1 \sin(at) + A_2 \cos(at) + A_3 \sin(2at) + A_4 \cos(2at) + A_5 x \sin(at) \\
& + A_6 x \cos(at) + A_7 y \sin(at) + A_8 y \cos(at) + A_9 x \sin(2at) + A_{10} x \cos(2at) + A_{11} y \sin(2at) + A_{12} y \cos(2at) \\
& + \frac{C_1 (t - t_0)}{(2000 - 1950)} + \frac{C_2 x (t - t_0)}{50} + \frac{C_3 y (t - t_0)}{50} + C_{\mathrm{SOI}} \mathrm{SOI}(t). \qquad (1)
\end{aligned}
$$

In (1) $x = (x - x_0)/2°$, $y = (y - y_0)/1°$, time t is in decimal year, $t_0 = 1975$, and SOI is a standardized and detrended 18-month-averaged Southern Oscillation index (SOI). The standardizing of the SOI followed the approach outlined by Trenberth (1984), maximizing the signal. Thus, the S_i regression coefficients fitted the mean ocean structure and its spatial gradients (S_{2-6}); the A_i terms fitted the seasonal cycle and its spatial gradients (A_{5-12}); the C_i coefficients fitted the nonseasonal temporal variability, with C_1 explicitly resolving the linear change with time and its spatial gradients (C_{2-3}); and the C_{SOI} coefficient resolved the ENSO footprint.

Two key assumptions underpin the model in (1). First, the seasonal cycle (both phase and amplitude) is constant over the 58 yr (1950–2008) of analysis. Second, the response of the ocean variable to ENSO is also linear and constant in time. The large number of parameters

TABLE 1. Comparison of the resolved trends of previous studies (scaled to compare to 1950–2000; original published values presented in parentheses along with the corresponding period of analysis) and those found in this study. This information has been provided to compare the sign and magnitude of signals found in this study to those of selected previous studies. While not an exhaustive list, studies that are not multidecadal in their comparison (<10 yr) were omitted from this comparison. Error estimates are presented at the 99% confidence interval.

Author/year	Location/water mass	Depth (m)	Equivalent magnitude (1950–2000)	This study
		Global		
Antonov et al. (2002)	Subtropics (40°S–40°N assumed)	0–400	+0.06 (0.02; 1978–94)	+0.018 ± 0.046
	Subpolar 50°–60°N	0–100	−0.12 (0.04; 1978–94)	−0.040 ± 0.055
	Subpolar 50°–60°N	100–1000	−0.06 (0.02; 1978–94)	+0.006 ± 0.052
	AAIW (Southern Hemisphere)	250–1000	−0.03 (<0.01; 1978–94)	−0.022 ± 0.023
Boyer et al. (2005)	Ross Sea 70°S, 165°E–136°W	0–2000	−	−0.081 ± 0.038
	Weddell Sea 70°S, 60°W–10°E	0–2000	−	+0.018 ± 0.031
	Subpolar 50°–70°N	0–2000	−	−0.026 ± 0.054
	Subtropics 20°–40°S	0–200	+	+0.028 ± 0.053
	Subtropics 20°–40°N	0–200	+	+0.010 ± 0.048
Helm (2008)	Upper thermocline, $\gamma = 24.8$ ($\gamma^a = 21$–24.8 assumed)	—	+0.14 (0.10; 1970–2005)	+0.122 ± 0.033
Hosoda et al. (2009)	Global 60°S–60°N	0–100	+0.01 (0.004 ± 0.056; 1975–2005)	+0.003 ± 0.057
	Southern subpolar 40°–60°S	0–100	−0.01 (0.018 ± 0.055; 1975–2005)	−0.044 ± 0.041
Roemmich et al. (2009)	AAIW (Southern Hemisphere)	100–1000	−	−0.040 ± 0.033
	Subtropics 20°–40°N	0–100	+	+0.004 ± 0.052
	Subtropics 20°–40°S	0–100	+	+0.031 ± 0.056
	Near equatorial 7°N	0–100	−	−0.034 ± 0.091
		North Atlantic		
Boyer et al. (2005)	Subtropics 20°S–20°N	0–500	+	+0.079 ± 0.055
	Subtropics 30°–40°N	200–500	−	+0.111 ± 0.040
	Subtropics 40°N	0–1500	>+0.03 (>0.0005 yr^{-1}; 1957–96)	+0.101 ± 0.038
	Subpolar gyre 45°–70°N	0–3000	>−0.03 (>0.0005 yr^{-1}; 1957–96)	−0.016 ± 0.041
Boyer et al. (2007)	North Atlantic and GIN seas (0°–70°N)	0–2000	−	+0.035 ± 0.043
Curry et al. (2003)	Subtropics 25°S–35°N	0–500	+0.17 to +0.67 (0.1–0.4; 1962–92)	+0.078 ± 0.054
	Subtropics 25°S–40°N	0–5500	+0.03 (0.02; 1962–92)	+0.051 ± 0.037
	Subpolar 40°–90°N	0–5500	−0.05 (0.03; 1962–92)	−0.002 ± 0.039
	Subtropics 30°–40°N ($\gamma^a = 27.8$ assumed)	—	+0.08 (0.05; 1962–92)	−0.025 ± 0.017
	Subtropics 25°S–30°N ($\gamma^a = 27.8$ assumed)	—	+0.03 to +0.07 (0.02–0.04; 1962–92)	+0.013 ± 0.007
Curry and Mauritzen (2005)	North Atlantic and GIN seas (55°–70°N)	—	−	−0.035 ± 0.045
Helm (2008)	Upper thermocline, $\gamma = 24.8$ ($\gamma^a = 21$–24.8 assumed)	—	+0.24 (0.17; 1970–2005)	+0.257 ± 0.236
Hosoda et al. (2009)	Equatorial 20°S–20°N	0–100	−0.02 (0.013 ± 0.079 1975–2005)	+0.153 ± 0.083
	Subtropical 20°–40°N	0–100	−0.12 (0.071 ± 0.080; 1975–2005)	+0.104 ± 0.053
	Subpolar 40°–60°N	0–100	−0.05 (0.028 ± 0.071; 1975–2005)	+0.057 ± 0.047
Grodsky et al. (2006)	Equatorial 15°S–15°N	0–5	+0.33 (0.2; 1960–90)	+0.182 ± 0.163
		South Atlantic		
Boyer et al. (2005)	AAIW	150–1000	−	−0.026 ± 0.063
Curry et al. (2003)	South of 25°S ventilated thermocline ($\gamma^a = 25.5$–27.0 assumed)	100–600	−0.42 (0.2; 1962–92)	−0.009 ± 0.093

TABLE 1. (*Continued*)

Author/year	Location/water mass	Depth (m)	Equivalent magnitude (1950–2000)	This study
	AAIW and UCDW (γ^a = 27–28 assumed)	—	−0.03 (0.02; 1962–92)	−0.004 ± 0.021
Helm (2008)	AAIW, 30°S–10°N, γ = 27.5	—	−0.04 (0.03; 1970–2005)	+0.017 ± 0.007
Hosoda et al. (2009)	Subtropical 20°–40°S	0–100	+0.11 (0.068 ± 0.065; 1975–2005)	+0.096 ± 0.090
		North Pacific		
Boyer et al. (2005)	North Pacific 15°S–60°N	0–300	>−0.03 (>0.0005 yr^{-1}; 1957–96)	−0.025 ± 0.048
	Subpolar 50°N	150	+	+0.076 ± 0.042
Cravatte et al. (2009)	West Pacific warm pool (annual climatology >28.5°C assumed)	0–10	−0.34 (1955–2003)	−0.182 ± 0.083
	West Pacific warm pool (annual climatology >29.0°C assumed)	0–10	−0.6 (1955–2003)	−0.219 ± 0.088
	West Pacific warm pool (surface density; 1°N, 156°W assumed)	0	−0.5 kg m^{-3} (1955–2003)	−0.54 ± 0.089 kg m^{-3}
Delcroix et al. (2007)	Subtropics 25°–27°N, 140°–150°E	0	−0.20 (0.12; 1970–2003)	−0.083 ± 0.039
	Tropics 1°N–1°S, 140°–160°E	0	−0.38 (0.23; 1970–2003)	−0.449 ± 0.090
Helm (2008)	Upper thermocline, 70°–0°S, γ = 24.8 (γ^a = 21–24.8 assumed)	—	−0.13 (0.09; 1970–2005)	+0.121 ± 0.076
	NPIW, γ = 26.8, 20°–35°N	—	−0.10 (0.07; 1970–2005)	−0.028 ± 0.011
Hosoda et al. (2009)	Equatorial 20°S–20°N	0–100	−0.06 (0.034 ± 0.041; 1975–2005)	−0.014 ± 0.071
	Subtropical 20°–40°N	0–100	−0.04 (0.022 ± 0.026; 1975–2005)	−0.062 ± 0.051
	Subpolar 40°–60°N	0–100	−0.10 (0.057 ± 0.049; 1975–2005)	−0.122 ± 0.057
Joyce and Dunworth-Baker (2003)	NPIW, γ = 26.8 (γ^a = 26.8, 20°–35°N assumed)	—	−0.07 (0.04; 1960–87)	−0.028 ± 0.011
Kouketsu et al. (2009)	24°N, NPIW minimum (γ^a = 26.4–27.2 assumed)	—	−0.01 (0.0045; 1985–2005)	−0.026 ± 0.011
	24°N, γ = >27.0	—	+	−0.003 ± 0.005
	24°N, γ = 25.8–26.9 (west of Hawaii)	—	−	−0.014 ± 0.021
	24°N, γ = >26.9 (west of Hawaii)	—	+	−0.005 ± 0.006
	24°N, North Pacific STMW (near North America, (γ^a = 25.2 assumed)	—	−(Very large)	−0.198 ± 0.069
	24°N, 140°–160°E	3000–5000	+	−0.003 ± 0.002
Roemmich et al. (2009)	West Pacific ITCZ	0–100	−	−0.134 ± 0.074
Wong et al. (1999)	Water column, 24°N	0–1400	−0.02 (0.0049; 1970–85)	−0.030 ± 0.032
	Water column, 10°N	0–1400	−0.004 (0.0016; 1969–89)	−0.021 ± 0.030
	NPIW, 47°N (γ^a = 26.4–27.2 assumed)	—	−0.26 (0.1; 1966–85)	+0.015 ± 0.018
	NPIW, 24°N (γ^a = 26.4–27.2 assumed)	—	−0.06 (0.017; 1970–1985)	−0.026 ± 0.011
		South Pacific		
Boyer et al. (2005)	Subtropics (20°–40°S assumed)	0–200	+	−0.006 ± 0.041
	Subtropics to 5°S (5°–40°S assumed)	>100–200	+	+0.020 ± 0.043
	AAIW	0–1000	−	−0.052 ± 0.031
Delcroix et al. (2007)	Tropics near equatorial 97°W	0	−0.53 (0.32; 1970–2003)	−0.074 ± 0.117
	Extratropics 15°–17°S, 170°E–170°W	0	−0.48 (0.29; 1970–2003)	−0.112 ± 0.062
Hill et al. (2008)	East Australian Current (EAC) 42.6°S 148.23°E	0	+0.15 (0.03 decade^{-1}; 1944–2008)	+0.165 ± 0.060
Hosoda et al. (2009)	Subtropical 20°–40°S	0–100	+0.08 (0.046 ± 0.048; 1975–2005)	−0.005 ± 0.044

TABLE 1. (*Continued*)

Author/year	Location/water mass	Depth (m)	Equivalent magnitude (1950–2000)	This study
Jacobs et al. (2002)	Ross Sea (65°–70°S, 170°E–140°W)	500	−0.18 (−0.003 yr^{-1}; 1963–2000)	+0.006 ± 0.029
Johnson and Orsi (1997)	AAIW 170°W, 48°S, γ = 26.8	—	−	−0.055 ± 0.019
Wong et al. (1999)	Water column, 17°S	0–1400	−0.01 (0.0068; 1967–94)	−0.013 ± 0.032
	AAIW, 17°S (γ^a = 27.1–27.6 assumed)	—	−0.04 (0.021; 1967–94)	−0.009 ± 0.004
		Indian		
Aoki et al. (2005)	UCDW, γ = >27.8–27.9 (60°–70°S, 30°–80°E)	—	+0.003 (0.0022 ± 0.001; 1957–96)	−0.003 ± 0.055
Bindoff and McDougall (2000)	AAIW, γ = >26.8 (20°–70°S, γ = 26.8–27.45 assumed)	—	−0.26 (0.13; 1962–87)	−0.032 ± 0.024
	AAIW, γ = >27.45 (20°–70°S)	—	−0.12 (0.06; 1962–87)	+0.015 ± 0.018
Boyer et al. (2005)	Basinwide	0–150	+	+0.001 ± 0.048
	>10°N	0–1000	+	+0.065 ± 0.031
	Subtropics 40°S–equator	>150	−	+0.028 ± 0.048
	AAIW	0–1100	−	−0.045 ± 0.035
	Subtropics 20°–40°N (<150 m assumed)	0–150	+	+0.144 ± 0.059
Helm (2008)	Upper thermocline, γ = 24.8 (γ^a = 21–24.8 assumed)	—	+0.13 (0.09; 1970–2005)	+0.08 ± 0.074
Hosoda et al. (2009)	Subtropical 10°–30°N	0–100	+0.01 (0.006 ± 0.069; 1975–2005)	+0.108 ± 0.077
	Equatorial 20°S–10°N	0–100	−0.01 (−0.005 ± 0.035; 1975–2005)	+0.019 ± 0.060
	Subtropical 20°–40°S	0–100	+0.01 (0.006 ± 0.061; 1975–2005)	+0.034 ± 0.046
Wong et al. (1999)	AAIW, 32°S (γ^a = 26.8–27.45 assumed)	—	−0.13 (0.064; 1962–87)	−0.071 ± 0.007

used to describe the mean and seasonal cycle are required as the spatial footprint of the data fitted can be large (Figs. 2a,c). Note that this model will not account for ocean responses that involve a time lag, as can be expected because of ocean wave dynamics associated with the ENSO. Thus, an 18-month smoother has been applied to the ENSO index so that only the low-frequency ENSO response is fitted.

The key advantage of this novel approach was the reduction of seasonal and spatial sampling bias, achieved by fitting the mean climatology and trends concurrently and removing bias due to sampling of strong ENSO cycles in the tropics. In the sparsely historically observed Southern Hemisphere oceans, the analysis relies on Argo's ability to highly resolve the mean, seasonal, and ENSO responses. This reduces aliasing by these observed phenomena into the multidecadal trend. The varied temporal global sampling also means that any ''simple'' average represents different eras in different parts of the ocean (Figs. 2b,d), and by fitting the trend and mean climatology at the same time, errors due to a biased climatology were avoided.

To further reduce outlier influences, a robust fitting algorithm (Holland and Welsch 1977) was used instead of the more sensitive linear least squares algorithm. This downweights the effect of outliers on the analyzed trend as the sum of absolute residuals rather than the sum of squared residuals is minimized. Each fit was performed

TABLE 2. Summary statistics for the three historical and Argo datasets.

Dataset	First year	Median year	Mean year	Last year	Total profiles	Unique profiles
SeHyD/IOHB	1875	1978	1977	2001	88 262	88 262
Hydrobase2	1874	1976	1973	2005	1 165 053	1 082 370
SODB	1910	1978	1977	2002	92 379	28 882
Argo	1995	2006	2006	2009	462 202	462 202
Total	1874	1984	1983	2009	1 807 896	1 661 716

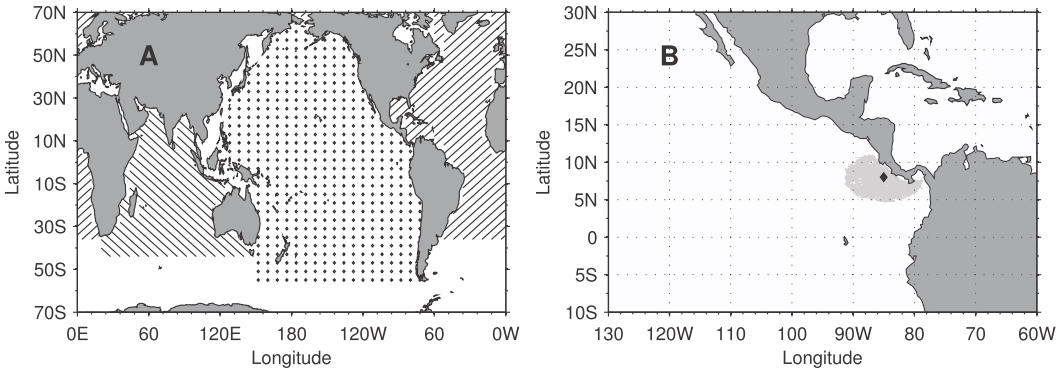

FIG. 1. (a) The gridpoint mask used in this study, note the exclusion of internal seas. Hashing indicates the basin labeling used to ensure fits do not mix data across land boundaries. Regions in the Southern Ocean with no hashing were sampled with no basin exclusions. (b) An example of the data selection region (light-gray area) for a surface grid point near the Isthmus of Panama, where application of the mask shown in (a) prevents the inclusion of Atlantic data in the analysis for this Pacific grid point.

twice, using the first fit to exclude points where fit residuals exceed five standard deviations, before then undertaking a second fit for each variable. A local standard error estimate was produced for each parameter in (1). Errors were also checked on a subset of the analyzed surfaces by bootstrapping the unfitted variance onto the original dataset to produce ensembles of 100 solutions. The statistics of these ensembles suggested that formal standard errors were generally well resolved, except in data-sparse, frontal, or eddy-rich regions, where they underestimated the standard error (standard deviation of the solution ensemble) by around 10%. Therefore, reported formal errors were increased globally by a representative factor (see following section on trend significance) to ensure standard error values were realistic.

Generally, the fitted fields were spatially smooth and well constrained. Visual inspection of the fitted parameters and the raw data revealed the dominance of eddy and seasonal signals in the upper ocean (Figs. 3c,d). However, on removing the mean and seasonal signals the multidecadal signal was clear in the raw data (Figs. 3a,b). The variance of the residuals largely reflect the locations of known ocean fronts, with active eddy fields or regions of strong F_W forcing such as the intertropical convergence zones (ITCZs) and regions such as the Bay of Bengal, which are subject to large terrestrial runoff events (Fig. 4a). We also examined errors on density levels (not shown). Errors were found to be approximately half the amplitude of the corresponding pressure analysis, primarily due to eddy heave (vertical heave of the water column) present in the pressure data, whereas heave does not play a large role on isopycnal coordinates.

To further highlight the changes on large spatial scales, all fields were smoothed before plotting using a 3-point boxcar filter, which is applied to the 1° latitude by 2° longitude grid.

4. Significance of resolved trends

A number of recent studies (e.g., Harrison and Carson 2007; Cravatte et al. 2009) describe limitations imposed by poor historical data records in temperature and salinity observations for the global and Pacific Oceans, respectively. However, these studies analyze the ocean in small spatial bins, increasing the chance of noise swamping a broad-scale trend signal.

The method employed here is tailored to resolve the linear trend of the large-scale pattern of 50-yr global salinity change. This method exploits all available regionally representative data for 1950–2008 to achieve this aim.

Statistical significance of these results was explicitly tested using a bootstrap technique for each latitude and longitude point at selected vertical levels on the regular grid. This was undertaken by perturbing the fitted observations using a random resampling with replacement of the unfitted residuals for each point (>1000 independent data points). An ensemble of 100 bootstrapped solutions was obtained, and the standard deviation of this bootstrapped ensemble was compared to the formal standard error produced by the robust fitter. For the analysis on pressure levels, the corresponding formal standard error underestimated the bootstrapped result by only 9% (globally averaged), with the density analysis underestimated by 10%. For both these analyses, larger error estimates were found on deeper levels as data coverage became sparser both temporally and spatially. A comparison was made with earlier analyses, which did not utilize the dual fitting algorithm (using the fit residuals to exclude points exceeding 5 standard deviations from the variable sample), with the initial exclusion (using the resolved residuals) halving the bootstrap-resolved underestimation—so from 23% to 9% for selected pressure levels.

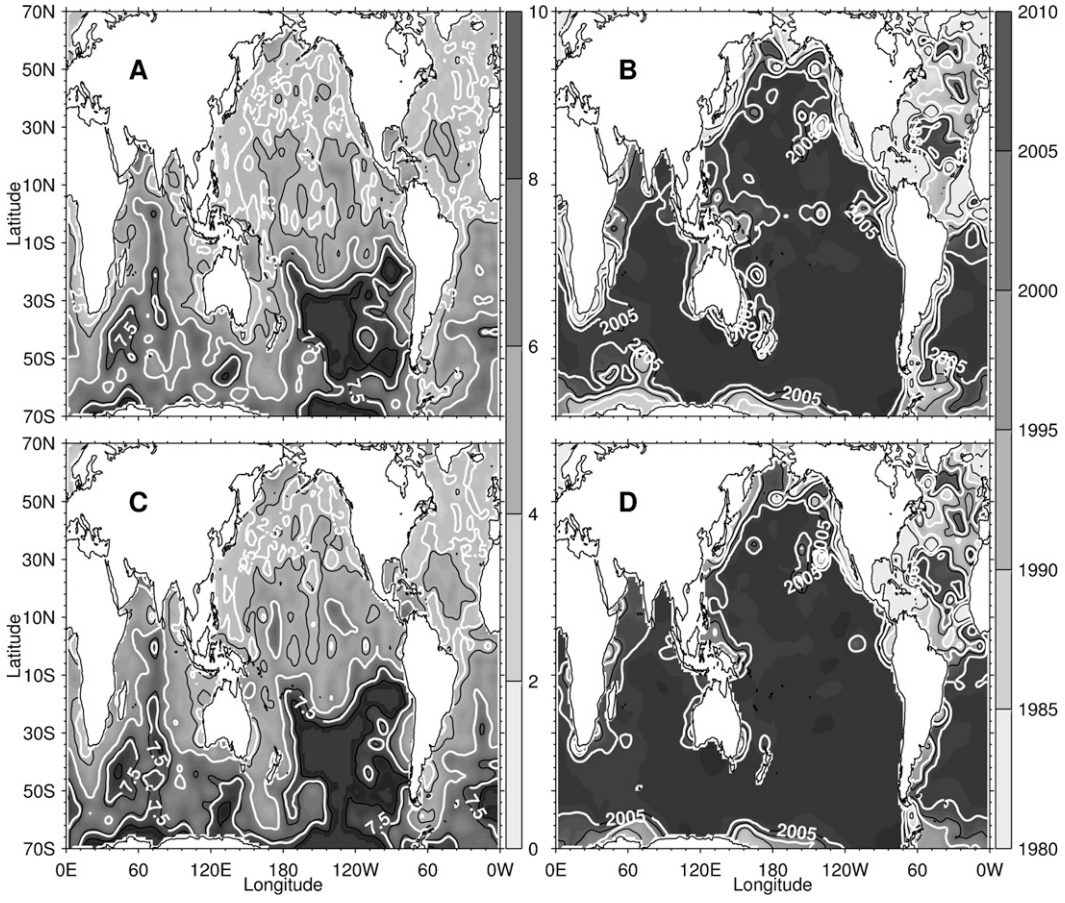

FIG. 2. Resolved metrics at the surface and 1000 dbar, which provide a visual representation of the available data coverage spatially and temporally for this analysis: standard deviation of (a) longitude at the surface (white contours indicate 2.5°, 5°, and 7.5°) and (b) 1000 dbar; and median (c) time at the surface (white contours represent the years 1985, 1995, and 2005) and (d) 1000 dbar.

Significance was calculated at the 99% confidence interval, which assumes a Gaussian distribution around the local sample mean, as there was no spatial structure or obvious biases present in the residuals. For basin-integrated results, the zonal-mean error was utilized, and significance was calculated at the 90% confidence level, as often zonal features such as the large freshening in the western Pacific and broad enhanced salinity in the eastern Pacific can cancel each other out in the resolved mean. Therefore, on the figures presenting trend results that follow in this study, stippling expresses regions where the signal is different from zero at the 99th (for vertical levels) and 90th (for basin integrals) percent confidence limit as described in figure captions. For result comparisons—see Table 1 and numerated descriptions within text—error estimates are expressed at the 99% confidence level.

Linear salinity changes for the 1950–2008 period of analysis will now be described. To simplify future comparisons changes are reported for the 50-yr period (nominally 1950–2000).

5. Surface changes

Diagnosed 50-yr linear trends of salinity at the surface (Fig. 5b) are large and coherent, with the spatial pattern of change strikingly similar to the mean surface salinity pattern (Fig. 5a), itself strongly resembling the F_W field (Fig. 5c). The 50-yr surface salinity changes are statistically significant at the 99% level over 43.8% of the global oceans.

Evaporation-dominated subtropical gyres in all oceans, particularly those in the Southern Hemisphere, show coherent salinity increases with values exceeding +0.20 (±0.081%; 99% confidence level) in the eastern South Pacific (14°S, 116°W), +0.34 (±0.041) in the subtropical South Atlantic (7°S, 16°W), and +0.45 (±0.12) in the subtropical North Atlantic (40°N, 48°W; Fig. 5b). Regions dominated by precipitation have undergone strong freshening. In the Atlantic, the region under the ITCZ freshens, but it is banded to the north and south by regions of very strongly increasing salinity (Fig. 5b). In

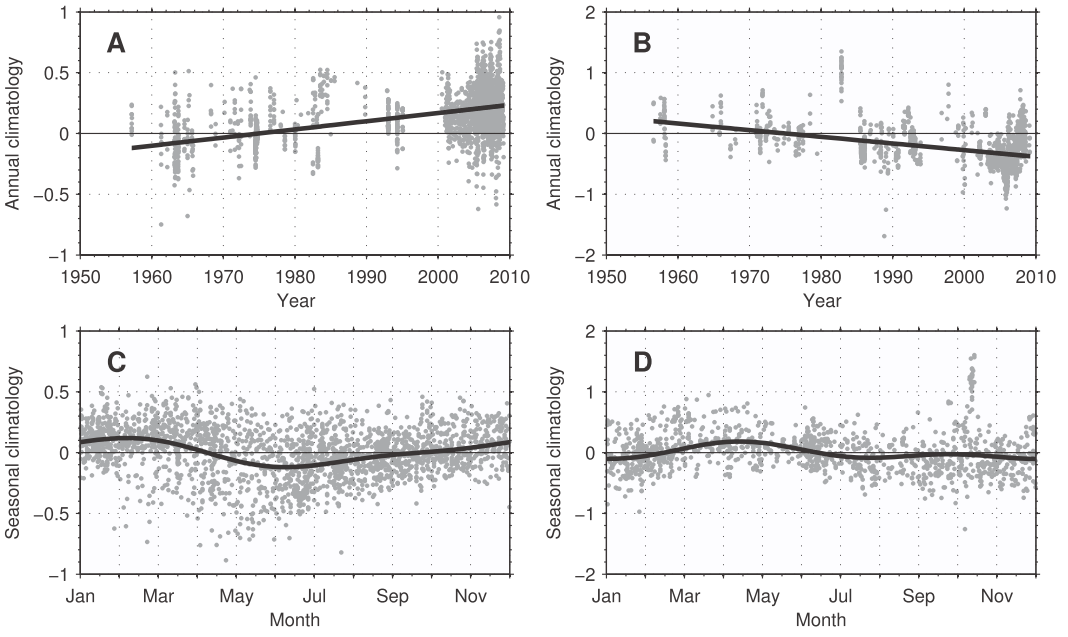

FIG. 3. Examples of raw data and the associated (a),(b) locally fitted linear trend and (c),(d) the seasonal cycle for the central equatorial South Atlantic [7°S, 16°W—(a),(c)] and the equatorial west Pacific warm pool [0°, 152°E—(b),(d)]. Fitted solutions (black) are compared with the data residuals (gray points): for (a) and (b) the residuals are plotted around the temporal mean, seasonal cycle, and SOI regression, whereas for (c) and (d) the residuals are plotted around the temporal-mean structure and SOI regression.

the western Pacific equatorial warm pool, large changes of −0.57 (±0.085) are found near the equator (2°S, 150°E; Fig. 5b).

It is noteworthy that the strong surface salinity contrast between the evaporative Arabian Sea and precipitation–runoff-dominated Bay of Bengal is also amplified over the 50-yr period. In the Arabian Sea, the maximum salinity increase is found along the northeast with a magnitude of +0.51 (±0.26) at 13°N and 74°E (Fig. 5b). In contrast, the Bay of Bengal shows a strong surface freshening signal of −0.40 (±0.31) found in the northeastern regions of the bay (19°N, 92°E; Fig. 5b). This freshening is constrained to the shallowest waters of the bay, with the signal reversing at 40-dbar depth (not shown). The freshening extends southward and crosses the equator with maximum surface amplitude south of India of −0.27 (±0.056) near 1°S and 80°E (Fig. 5b).

The globally averaged surface salinity change is small (+0.0024 ± 0.051), whereas basin averages are more noteworthy: enhanced salinity for the Atlantic (+0.078 ± 0.095), freshening in the Pacific (−0.044 ± 0.064), and a near-neutral result for the Indian Ocean

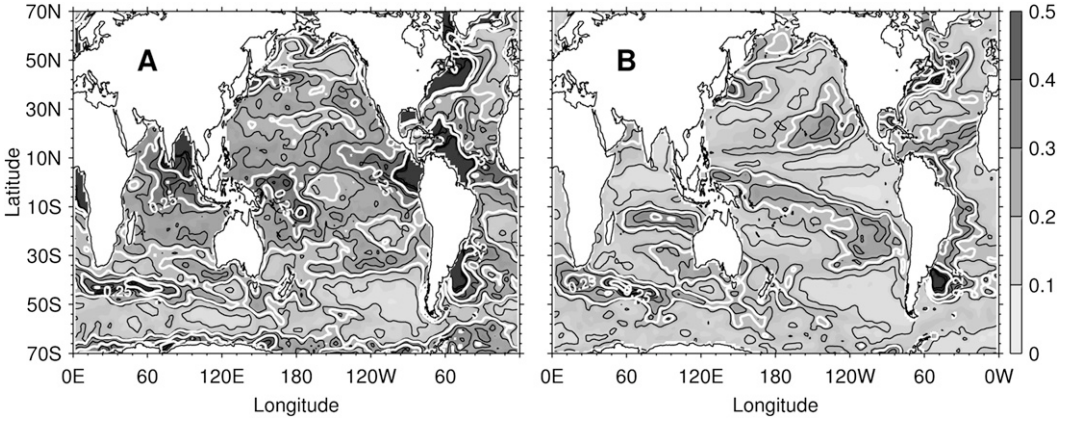

FIG. 4. The standard deviation of the residuals to the full parametric fit undertaken in pressure coordinates at (a) the surface and (b) 200 dbar (0.125-, 0.25-, and 0.375-pss contour is in white, black contour interval is 0.1).

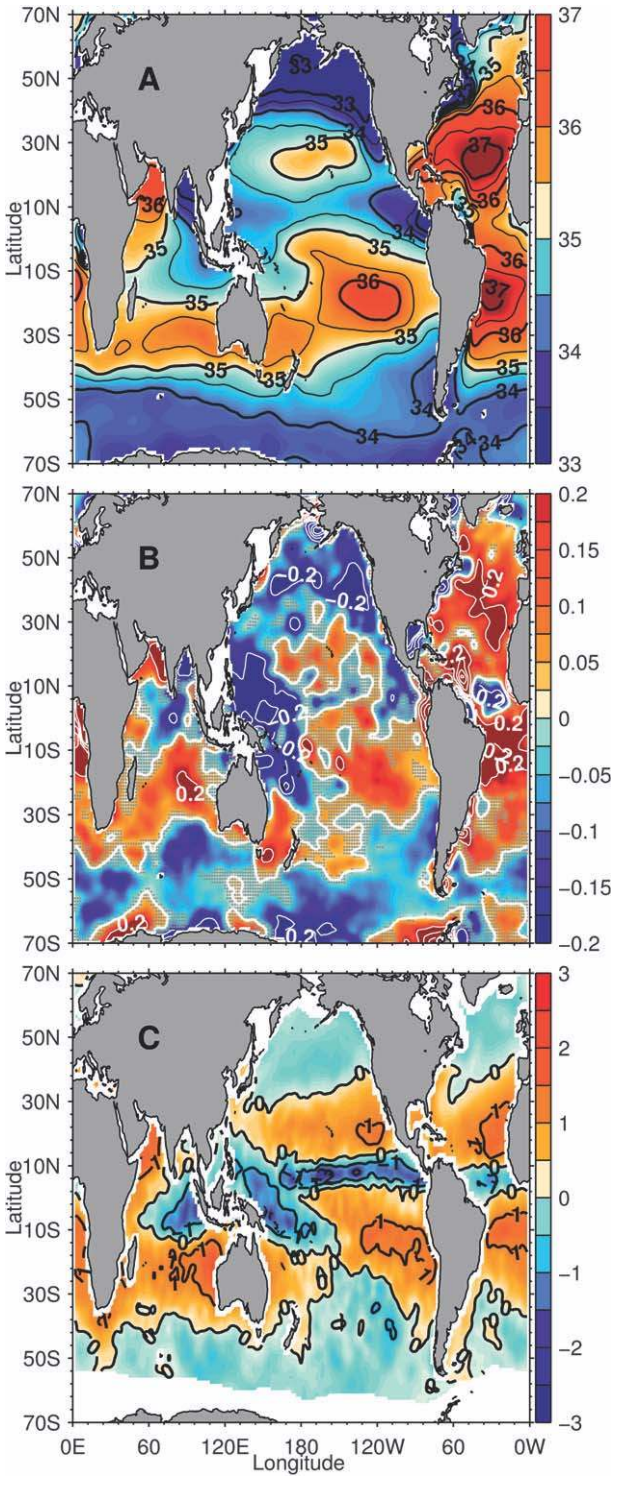

FIG. 5. (a) The 1950–2000 climatological-mean surface salinity. Contours every 0.5 pss are plotted in black. (b) The 50-yr linear surface salinity trend [pss (50 yr)$^{-1}$]. Contours every 0.2 are plotted in white. Regions where the resolved linear trend is not significant at the 99% confidence level are stippled in gray. (c) Ocean–atmosphere freshwater flux (m^3 yr^{-1}) averaged over 1980–93 (Josey et al. 1998). Contours are every 1 m^3 yr^{-1} in black.

(-0.001 ± 0.061). Thus, an amplification of existing interbasin-mean salinity contrasts is apparent, reflecting a strengthening of the mean surface salinity pattern. This corresponds strongly with expectations of an intensification of the hydrological cycle in a warmer world (Solomon et al. 2007; Held and Soden 2006).

6. Subsurface changes

Global zonally averaged 50-yr salinity changes on pressure surfaces are similar to those found in previous studies in the upper ocean with consistent agreement (Table 1), though the magnitudes diagnosed are frequently larger and the resolved change patterns are more spatially coherent (Fig. 6). Enhancements to the salinity maxima in the subtropical gyres are presented by this study, in agreement with Boyer et al. (2005); however, this study finds a stronger and broader freshening in the Southern Ocean following the equatorward spreading of the AAIW salinity minimum near 1000 dbar (Fig. 6). This analysis also features a freshening of the shallow tropical freshwater pool near the equator, a feature not evident in Boyer et al. (2005). In addition, increased salinity along 1000 dbar in the Northern Hemisphere is resolved with an apparent enhancement of the Mediterranean Outflow Waters (MOW) signature, following circulation pathways southward (Fig. 6a; Curry et al. 2003; Rohling and Bryden 1992; Roether et al. 1996; Lascaratos et al. 1999). The large, broad freshening featured in the high-latitude Northern Hemisphere in Boyer et al. (2005) is not reproduced by this study (Fig. 6), and in their result is potentially due to aliasing by the strong decadal temporal variability found in the North Atlantic (see Dickson et al. 1988 and Belkin et al. 1998).

Understanding salinity changes in the subsurface ocean is dependent on a decomposition of two contributing processes on a pressure surface: vertical (or lateral) heave of isopycnals due to dynamic processes such as wind field changes and modification of the temperature–salinity (T–S) relationship along isopycnals largely driven by F_W changes or mixing processes along the water-mass pathways, as discussed by Bindoff and McDougall (1994) and Helm (2008). Using the dual analysis on both pressure and density surfaces allows for a direct calculation of the component of salinity change on pressure accounted for by the local vertical heave of isopycnals and that which is due to changes in the T–S relationship. A decomposition of the total salinity changes on a pressure surface dS_p over the analysis period can now be described as follows:

$$dS_p = dS_{\gamma^a} + \frac{\partial \overline{S}}{\partial \overline{\gamma^a}}\, d\gamma_p^a, \qquad (2)$$

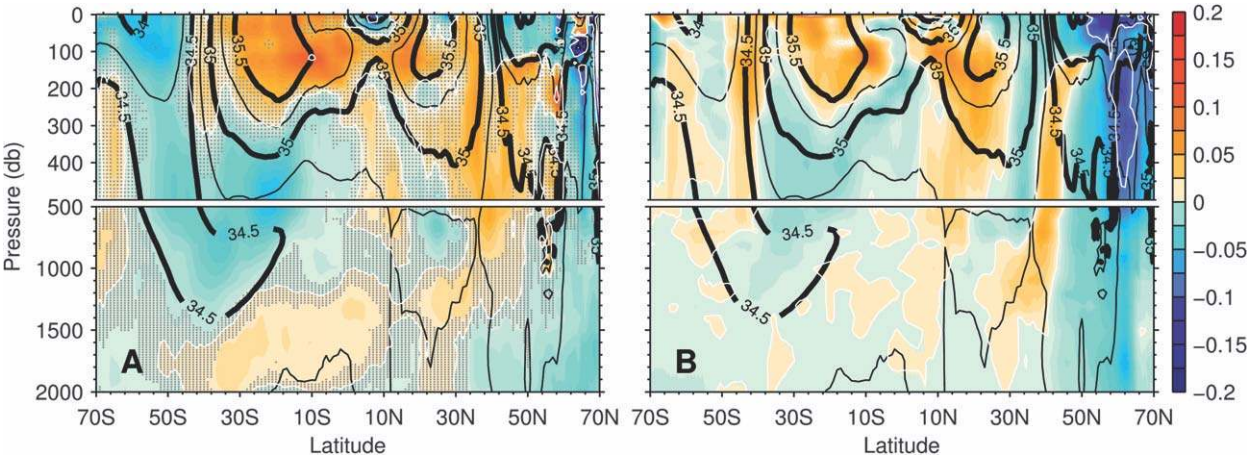

FIG. 6. (a) Global zonally averaged linear salinity trends [pss (50 yr)$^{-1}$] analyzed on pressure surfaces (colors with white contours every 0.1) in this study. (b) Regions where the resolved linear trend is not significant at the 90% confidence level are stippled in gray, from the dataset of Boyer et al. (2005). Mean salinity resolved in this study is contoured in black: 0.5 pss for thick lines and 0.25 for thin lines.

where dS_{γ^a} represents salinity changes on density levels, $\partial\overline{S}/\partial\overline{\gamma^a}$ represents the local gradient of mean salinity against density, and $d\gamma_p^a$ represents the density change on a pressure surface.

Heave-driven salinity changes [second term in (2)] are large in every basin (Figs. 7b,e,h), particularly in the strongly warming Atlantic, where deepening isopycnals dominate the salinity change on a pressure surface above 500 dbar (cf. Figs. 7a,b). Heave-driven changes also drive a consistent dipole of salinity change around the salinity minimum of the AAIW (γ^a = 27–27.5 kg m^{-3}; Hanawa and Talley 2001; Talley 2003) in every Southern Hemisphere basin between 50° and 60°S, with increased salinity above the minimum and decreased salinity below it (Figs. 7c,f,i), expressing a deepening and southward shift of the minimum core.

Salinity changes diagnosed on a density surface more clearly reveal changes to the ocean water masses by removing the local heave effect. When density changes are expressed on their corresponding pressure levels (Figs. 7c,f,i), they reveal a stronger connection between near-surface changes and those found in the ocean interior, where subpolar and subtropical surface changes appear to penetrate equatorward along isopycnals in agreement with the ventilation of the subtropical thermocline (Luyten et al. 1983).

Consistent patterns of salinity change are found independently in every ocean basin. A surface-sourced freshening centered on 50°S in the density ranges of the Subantarctic Mode Waters (SAMW; γ^a = 26–27 kg m^{-3}) penetrates to the equator in every southern gyre. A strong equatorward freshening plume is also seen on lighter levels in the North Pacific Central Waters, found between the shallow salinity maxima and intermediate water salinity minima (Fig. 7f). The salinity maximum waters of the upper ventilated thermocline generally increase in salinity for all gyres and all basins.

Chlorofluorocarbon-11 (CFC-11), an anthropogenic tracer, marks ocean waters that have ventilated to the atmosphere since the mid-1960s (Bullister 1989; Figs. 7c,f,i). Salinity changes on density surfaces in nearly all basins are very small in regions that were unventilated during the analysis period (with consequently near-zero CFC-11 concentrations), such as the Pacific and Indian Oceans below 1000 dbar. Exceptions are the consistent and significantly increased salinity found in the deep Atlantic (Figs. 7a,c) and increased salinity in the northern Indian Ocean (Figs. 7g,i). The water masses in both these regions are impacted by highly saline marginal sea overflows [MOW for the Atlantic; Red Sea (RSW) and Persian Gulf Water (PGW) for the Indian Ocean]. A possible explanation is that these high-salinity-concentrated overflows are driving strong salinity changes while introducing only small quantities of the CFC-11 tracer.

7. Isopycnal-following surface analysis

Large and coherent changes of salinity are found on subsurface isopycnals as established in previous studies (e.g., Bindoff and McDougall 2000; Curry et al. 2003; Helm 2008; Wong et al. 1999). In some regions, these appear related to F_W changes at the ocean surface. For example, Bindoff and McDougall (2000) described subsurface changes derived from Indian Ocean hydrographic data and attributed changes in SAMW and AAIW salinities to warming and freshening, respectively. In their analysis, only vertical heave or compensating cooling–freshening

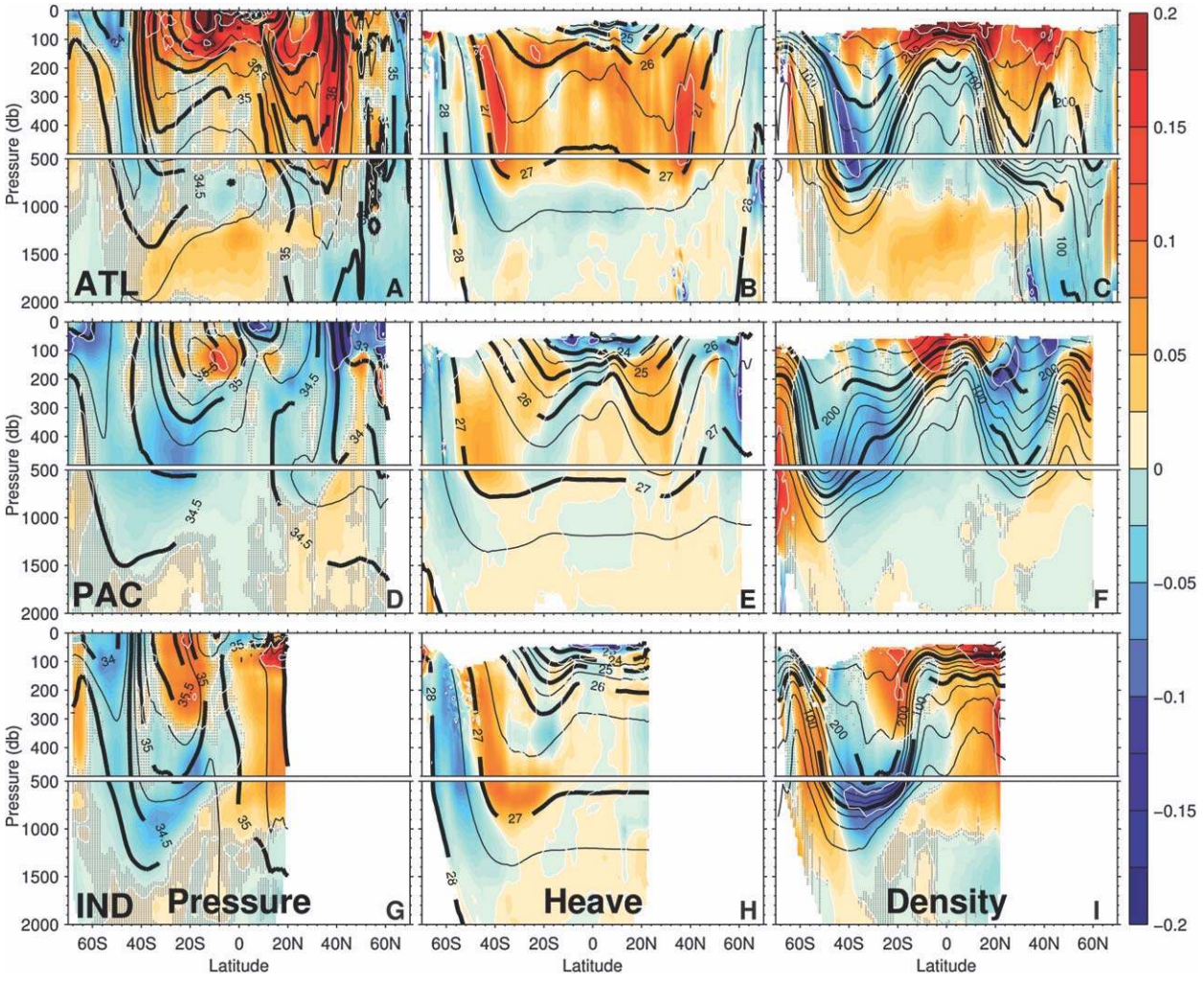

FIG. 7. Zonally averaged salinity trends (colors) for (a),(b),(c) the Atlantic, (d),(e),(f) Pacific, and (g),(h),(i) Indian Oceans. White contours highlight salinity changes every 0.1 pss (50 yr)$^{-1}$. (left) Trends are on pressure surfaces and mean salinity are overcontoured in black (every 0.25, bolded every 0.5). Regions where the resolved linear trend is not significant at the 90% confidence level are stippled in gray. (middle) Calculated heave-driven salinity changes (see text), and mean density is overcontoured in black (every 0.5 kg m^{-3}, bolded every 1 kg m^{-3}). (right) Salinity changes analyzed on density surfaces and mapped back to pressure with CFC-11 concentrations overcontoured in black (every 25 pmol kg^{-1}, bolded every 100 pmol kg^{-1}). Regions where the resolved linear trend is not significant at the 90% confidence level are stippled in gray. Note the change in vertical scale between 0–500 and 500–2000 dbar for upper and lower panels, respectively.

(preserving the local vertical T–S relationship) is considered. The current analysis deduces the critical importance of *lateral* isopycnal migration through ocean surface climate zones, with these migrations driving changes in the T–S relationships subducted at isopycnal outcrops. The consequence of such lateral migrations may lead to a lower (or higher) salinity being subducted into the interior ocean along any particular isopycnal; even with a fixed surface salinity regime (thus no F_W changes are required).

Changes in the mean location of isopycnal outcrops are calculated using the analysis of surface density trends. Using the resolved mean seasonal cycle and 50-yr trend analysis, winter (permanent) isopycnal outcrops are located for the years 1950 and 2000 (Fig. 8). Significant lateral shifts (50–100 km) are found for nearly all outcrops—predominantly a poleward migration. Comparison of the thermal versus haline contributions (not shown) indicates the migration is driven largely by the broad-scale ~0.5°C surface warming occurring over this period (Solomon et al. 2007). In some regions, such as the western Pacific warm pool, where strong freshening coincides with warming, outcrops have migrated even further—both poleward and zonally (Fig. 8). Here, the magnitude of the freshening, coupled with the localized warming (not shown), leads to a broad expansion of the

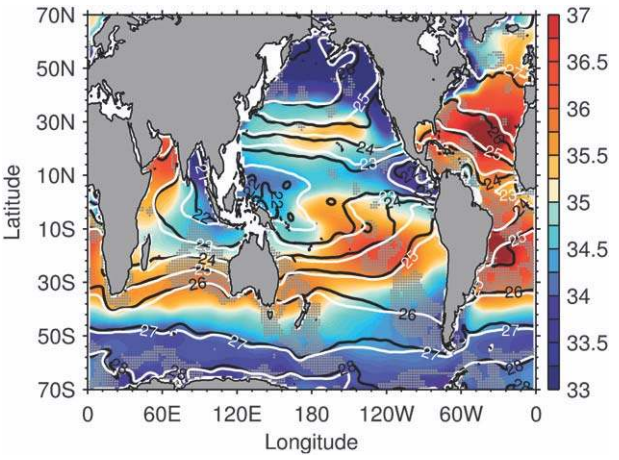

FIG. 8. Maximum winter surface density in 1950 (black lines) and nominally 2000 (white lines) overlaying the climatological-mean salinity (colors). Regions where the resolved linear trend for surface density changes is not significant at the 99% confidence level are stippled in gray.

surface region represented within the confines of the 22.0 kg m^{-3} isopycnal. The reduction of surface density peaks at -0.54 kg m^{-3} (± 0.041; 1°N and 156°E).This large deviation is clearly visible as a surface isopycnal outcrop migration (Fig. 8) and persists to 80-dbar depth (density and stratification changes will be described elsewhere). This regional density change agrees with the result of Cravatte et al. (2009) within error estimates (Table 1).

Because meridional gradients in the mean salinity field are very strong (Fig. 8), migrating outcrops have thus experienced large changes in their mean surface salinity regime, with this change signal then carried into the interior ocean by ocean subduction. The total surface salinity is defined as $S = S' + \overline{S}$, where S' is the 50-yr temporal perturbation, and $\overline{S}$ is the 50-yr climatological mean. For a given isopycnal outcrop at a meridian, the total surface salinity change is thus

$$\left.\frac{dS}{dt}\right|_{\gamma^a,x} = \left.\frac{d\overline{S}}{dt}\right|_{\gamma^a,x} + \left.\frac{dS'}{dt}\right|_{\gamma^a,x} \cong \left.\frac{\partial \overline{S}}{\partial y}\frac{dy}{dt}\right|_{\gamma^a,x} + \left.\frac{\partial \overline{S}}{\partial t}\right|_{y,x} + \left.\frac{dS'}{dt}\right|_{\gamma^a,x}.$$

As zonal gradients in salinity are smaller than meridional gradients, and as most outcrop migrations are poleward, salinity changes associated with zonal outcrop migration have been ignored. Because $(\partial \overline{S}/\partial t)\big|_{y,x}$ is zero by definition, the change following an outcrop is estimated as

$$\left.\frac{dS}{dt}\right|_{\gamma^a,x} \cong \left.\frac{\partial \overline{S}}{\partial y}\frac{dy}{dt}\right|_{\gamma^a,x} + \left.\frac{dS'}{dt}\right|_{\gamma^a,x}, \quad (3)$$

where $[(\partial \overline{S}/\partial y)(dy/dt)]\big|_{\gamma^a,x}$ is the salinity change at the outcrop due to a meridional shift $(dy/dt)|_{\gamma^a,x}$ (generally poleward) through the mean surface salinity field ($\overline{S}$). Hereafter, the lhs of (3) is referred to as the *total* salinity change at the outcrop, which captures surface salinity changes including F_W changes, whereas the first term on the rhs will be referred to as the *migration-driven* change, which we describe as largely due to broad-scale warming occurring across the global ocean.

Both rhs terms in (3) are important. When outcrops migrate into a higher mean salinity zone (e.g., toward the surface salinity maximum in subtropical gyres), more saline water is subducted, whereas those migrating poleward and away from the subtropical maxima subduct fresher waters. These migration-driven changes are modified by the second rhs term in (3)—the temporal change of the surface salinity field, likely due to F_W changes.

In practice, using the outcrop locations in 1950 and 2000 (Fig. 8), and both the mean and perturbation salinity fields, the total surface 50-yr salinity changes are determined on the longitudinal grid of the analysis—the lhs of (3). The meridional migration-driven salinity changes are similarly calculated based on the outcrop locations and mean salinity field alone—the first term on the rhs of (3). For presentation, these salinity changes at the outcrops are then averaged in 6° longitudinal bands (Fig. 10) or used to form an outcrop-following zonal mean for each basin (Fig. 9). These components of salinity change as the outcrops can now be compared to the independently analyzed subsurface changes on isopycnals. This enables an exploration of how surface changes may be driving changes in the ocean interior as circulated by the mean flow.

8. Kinematics of changes found on subsurface isopycnals

Zonally averaged salinity changes on isopycnals for each basin show a remarkably similar relationship to analyzed changes at the outcrops (Fig. 9). There is a striking relationship between the mean salinity field and the 50-yr salinity change on isopycnals. In every subtropical gyre, widespread increases in salinity occur in the upper thermocline, with the largest salinity change signal near the subtropical density outcrops. In the central waters (we use this general term to describe the waters that lie between the shallow subtropical maxima and intermediate water salinity minima; $\gamma^a < 27.25$ kg m^{-3}), a widespread freshening signal dominates in every gyre. Note that each subtropical gyre operates on its own native density range, and thus the central water in the south Indian Ocean is found on comparatively denser

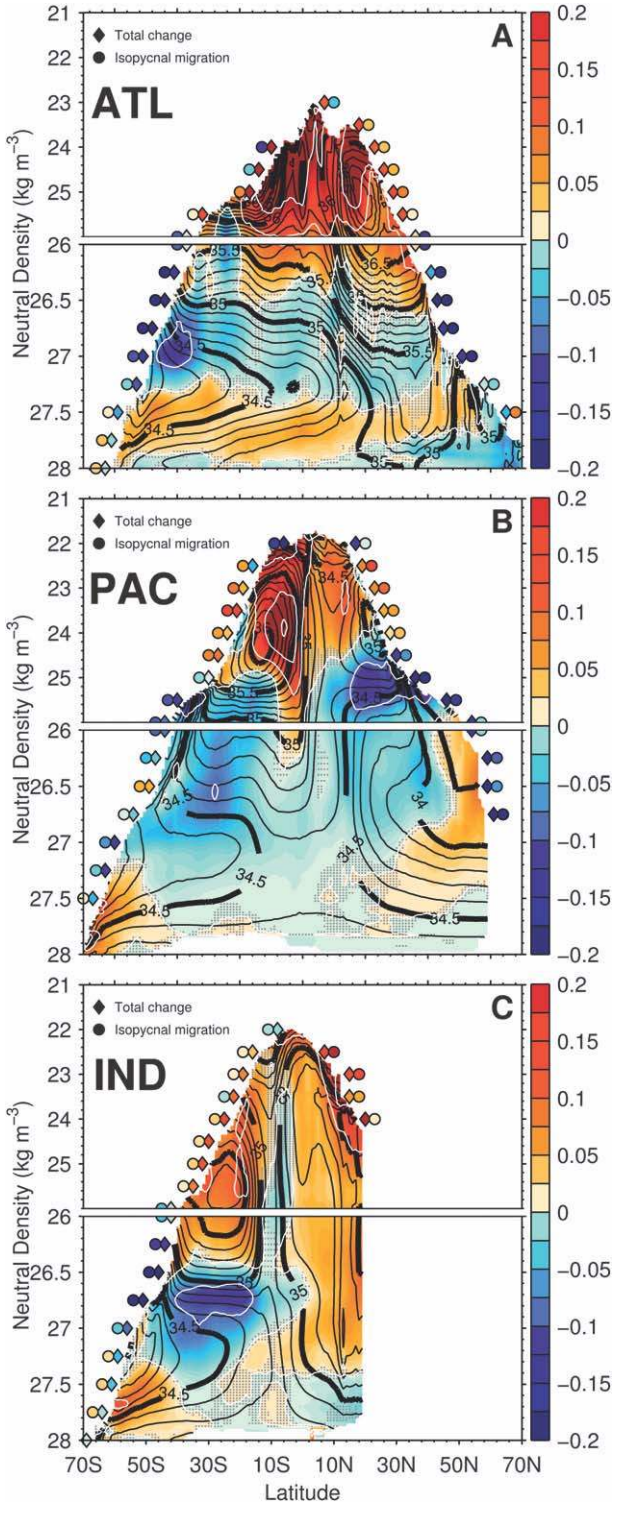

FIG. 9. Zonally averaged linear salinity trends [colors, pss (50 yr)$^{-1}$] analyzed on isopycnals for the (a) Atlantic, (b) Pacific, and (c) Indian Oceans. White contours represent salinity changes every 0.1 pss. Values on surfaces lighter than the winter outcrop have been blanked. Climatological-mean salinity is overcontoured in black every 0.1, bolded every 0.5. Plotted in colored symbols along the winter outcrop positions are zonally averaged linear salinity trends due to the total (see text) salinity change (diamonds) that is due only to meridional isopycnal migration (circles). Note the change in vertical scale between 21–26 and 26–28 kg m^{-3} for upper and lower panels, respectively. Regions where the resolved linear trend is not significant at the 90% confidence level are stippled in gray.

surfaces than the central water in the fresher North and South Pacific, for example. Despite these regional differences, a common and widespread central water freshening is found on the density classes appropriate for each basin.

Surface-deduced salinity changes at the outcrop reveal that total salinity changes (diamonds in Fig. 9) also show a general freshening at the central water outcrops. Subduction of this strong surface change at outcrops by normal ocean ventilation can explain the pattern of subsurface central water freshening. Furthermore, a large portion of the freshening at the outcrops is driven by meridional isopycnal migration (circles in Fig. 9). Thus, these suggest that the broad-scale surface warming of the global ocean has driven isopycnal outcrops poleward. In the case of central waters, this has shifted them into a fresher mean salinity regime, where waters subducted in 2000 are fresher than those subducted in 1950. Because ocean surface warming is comparatively uniform and widespread (Solomon et al. 2007), this phenomenon is repeated in each basin's subtropical gyre.

General increases in isopycnal subsurface salinity in all subtropical gyres (Fig. 9) are observed for densities near to, and lighter than, the shallow salinity maxima. Again, poleward isopycnal migration (in this case, *toward* the surface salinity maxima) can account for this common signal. In the south Indian subtropical gyre, however, the total increase at the outcrop is larger than the isopycnal migration change, implying that F_W-driven salinity changes dominate here. A general agreement between the changes diagnosed at the surface and the independently analyzed subsurface features are found, implying propagation of outcrop salinity anomalies along isopycnals into the ocean interior in the actively ventilating subtropical gyres.

Salinity changes are generally weak in the deep waters of the tropics and subtropics, on surfaces denser than the central waters ($\gamma^a > 27.25$ kg m^{-3}; Fig. 9), and regions occupied by the poorly ventilated upper deep waters (UDW) of the Pacific and Indian Oceans. Two exceptions exist, however, both occurring where waters are influenced by high-salinity marginal sea overflows:

MOW for the Atlantic, and RSW and PGW in the northern Indian Ocean, respectively.

Widespread increases in salinity in the UDW below the AAIW minima (γ^a = 27.5–27.75 kg m^{-3}) in the Atlantic basin are observed where low CFC-11 concentrations exist (Figs. 7c and 9a), a result also found by Curry et al. (2003). The interior ocean waters in this density range are greatly influenced by the high-salinity MOW (Candela 2001), and it is plausible that longer-term changes in MOW are driving salinity changes at these densities. Because of their small volume to surface area, marginal sea waters will tend to respond to F_W changes more strongly than the open ocean. A projected decrease to precipitation in the already evaporation-dominated Mediterranean region is expected in the twenty-first century, a result of anthropogenic climate change (Bethoux et al. 1998; Giorgi and Lionello 2008; Sanchez-Gomez et al. 2009). Rohling and Bryden (1992) and Roether et al. (1996) have documented enhanced salinity changes in the western and eastern Mediterranean, respectively. Rohling and Bryden (1992) found consistent salinity increases in deep waters, with a near-threefold acceleration in the rate of salinity change around 1955 extending into the late 1980s, when compared to the earlier period 1900–55. They found salinity increases recorded back to 1909, suggesting that MOW changes in the extended Atlantic could have been forced by pre-1950 changes in the Mediterranean water balance, possibly due to land use changes.

Similar salinity increases occur in the poorly ventilated deep north Indian Ocean (Fig. 9c) across the density range influenced by the RSW and PGW overflows (Tomczak and Godfrey 1994). It is striking how the spatial extent of the 50-yr change largely coincides with the mean saline plume of RSW (near γ^a = 27.3 kg m^{-3}; Beal et al. 2000; Fig. 9c).

Another globally distributed deep-water change is an increase in salinity between 50° and 60°S in the UCDW in all basins. This follows the result documented by Aoki et al. (2005) for the high-latitude south Indian Ocean (Fig. 9). The observed change occurs on isopycnals influenced by Ekman suction (Tomczak and Godfrey 1994). In this upwelling zone, no correspondence between surface-deduced changes and subsurface changes are found (Fig. 9). Instead, this circumpolar increase in salinity in high southern latitudes (Fig. 9) is likely to reflect a southward shift in the Antarctic Circumpolar Current (ACC; Gille 2002; Alory et al. 2007) and its water-mass fronts.

In summary, all ocean basins show a freshening of central waters on isopycnals and increases to salinity in the subtropical waters—a phenomena common to all subtropical gyres, which to first order is likely a result of the subduction of a broad-scale and widespread surface warming observed over the last 50 yr (Solomon et al. 2007). Warming-driven isopycnal migration produces the largest changes at outcrops where the surface meridional salinity gradients are strongest. Thus, the 50-yr salinity changes reach maximum values where mean salinity–density gradients are strongest (Fig. 9). Second-order changes are likely a result of surface flux changes, with the largest changes observed in the subtropical Atlantic and Indian Ocean basins (diamonds versus circles in Figs. 9a,c).

While the basin zonal averages (Fig. 9, and associated pressure analysis—Figs. 7a,d,g) reveal a distinct inter-basin symmetry, both the mean surface salinity and the F_W patterns have a rich longitudinal structure (Figs. 5a,c), which is lost by zonal averaging. Therefore, the full three-dimensional nature of the subsurface salinity changes and their relationship to changes at the outcrops and ocean circulation pathways will now be explored.

9. Water-mass changes

a. Upper thermocline γ^a = 24 kg m^{-3}

The largest subsurface salinity changes are found on the upper-thermocline isopycnals, where faster ventilation times quickly propagate surface changes into the interior (Fig. 10a). The γ^a = 24 kg m^{-3} isopycnal outcrops near 20° in both the Pacific and Indian Oceans and deepens to near 100 dbar near the equator (Figs. 7b,e,h). In the Atlantic basin, which operates in a comparatively denser regime, this isopycnal outcrops equatorward near 10°S and 15°N.

Large salinity increases occur on this surface across the entire tropical Atlantic basin (Fig. 10a). At the outcrop location, the total salinity change (diamonds in Fig. 10a) predicts the subsurface increase and isopycnal migration (circles in Fig. 10a) accounts for very little (and in some instances is opposite in sign). Consequently, increased surface salinity must be largely responsible for this tropical shallow Atlantic thermocline increase.

The Pacific basin reveals strong longitudinal variations in changes on this γ^a = 24.0 kg m^{-3} surface (Fig. 10a). Both northern and southern gyres feature plumes of increased salinity extending westward toward the equator from the midbasin outcrop, following the known geostrophic flow pathways (Luyten et al. 1983). East of these plumes, a weaker freshening penetrates the gyres near the outcrops. Much of the subsurface change corresponds to the surface analysis that, in contrast to the Atlantic, is dominated by isopycnal migration (circles in Fig. 10a). The stronger increase of the South Pacific salinity maximum over the past 50 yr has resulted in an increased

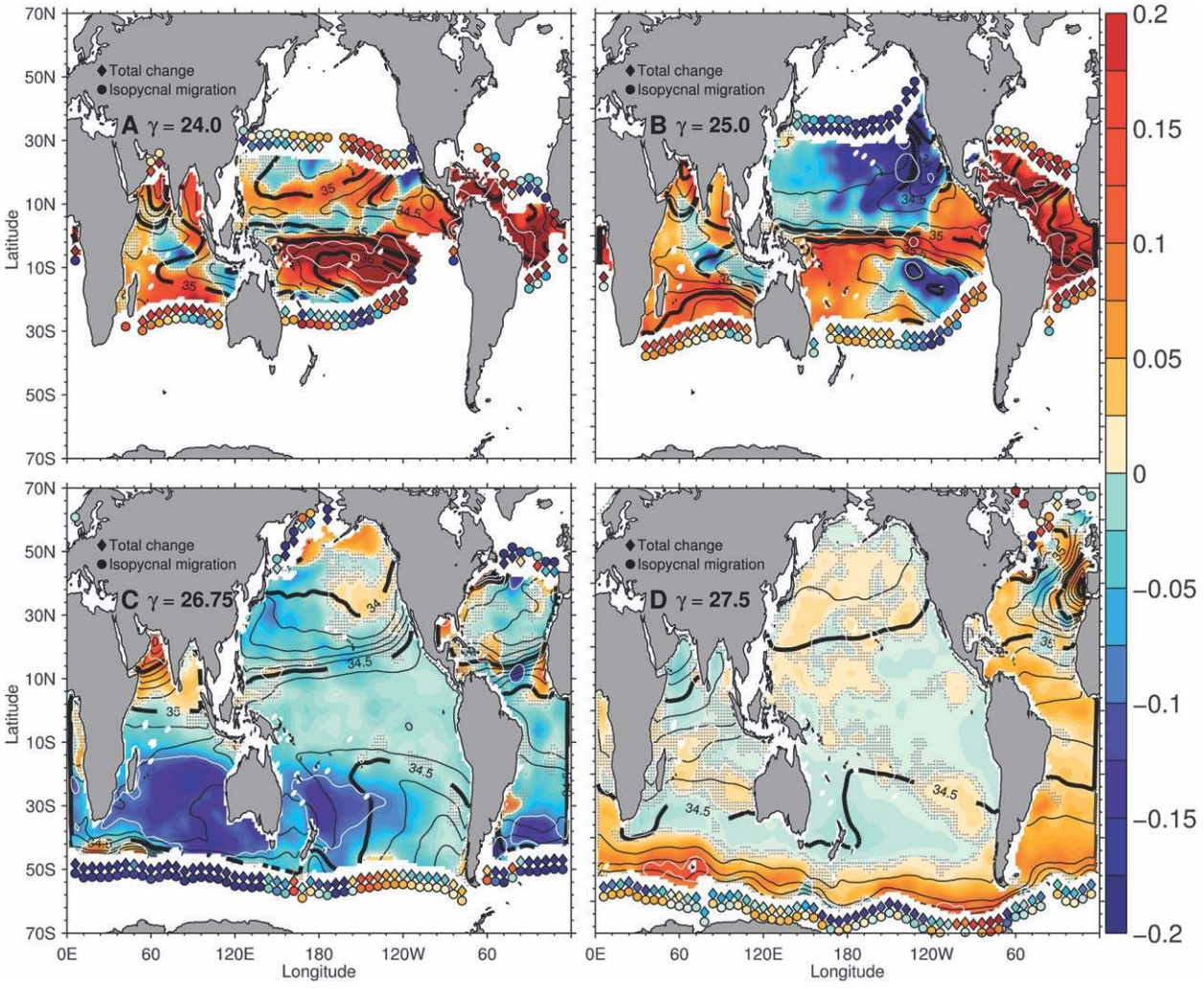

FIG. 10. The salinity trend [pss (50 yr)$^{-1}$] on isopycnal surfaces (a) 24.0 and (b) 25.0 kg m^{-3}. White contours are plotted every 0.25. Climatological-mean salinity is overcontoured in black every 0.25 pss and bolded every 0.5 pss. Salinity trend [pss (50 yr)$^{-1}$] for isopycnals (c) 26.75 and (d) 27.5 kg m^{-3}. Salinity mean is contoured. Climatological-mean salinity is overcontoured in black every 0.1 and bolded every 0.5. The colored symbols are as in Fig. 9 and described in the text. Regions where the resolved linear trend is not significant at the 99% confidence level are stippled in gray.

meridional salinity gradient at the equator in the western Pacific in the core of the equatorial Undercurrent (EUC). It is therefore likely that the salinity increase found in the eastern equatorial Pacific just north of the equator may be attributable to the outflow of a more saline EUC, whose waters are known to flow both north and south of the equator upon termination (Tsuchiya 1968).

In the shallow Indian Ocean, thermocline increased salinity is observed almost everywhere, except for a freshening aligned with the Indonesian Throughflow (ITF) plume extending from the east along 12°S and in the central region south of the equator. In the south Indian subtropical gyre, where this $\gamma^a = 24.0$ kg m^{-3} surface outcrops, uniform increases are observed, driven largely by surface salinity changes and not outcrop migration (diamonds in Fig. 10a). Indeed, this outcrop has migrated little in the central and eastern basin (Fig. 8), implying that the large surface salinity change (Fig. 5b) coincides with a density-compensating warming (not shown).

b. *Lower thermocline* $\gamma^a = 25$ kg m^{-3}

The $\gamma^a = 25.0$ kg m^{-3} surface lies in the lower thermocline in most basins, outcropping near 30° in both the Pacific and Indian Oceans and deepening to near 150 dbar on the equator (Figs. 7b,e,h). In the Atlantic basin, this surface outcrops near 15°S and 20°N (Fig. 10b).

In the Atlantic on this surface, again, the largest changes are found. A basinwide salinity increase is observed, largely accounted for by changes at the outcrop that are only partly migration driven (Fig. 10b). In stark contrast, the North Pacific shows a strong and widespread freshening, which is intensified eastward from the central Pacific near the outcrop (Fig. 10b). The surface analysis shows that outcrop migration (circles in Fig. 10b) is driving this widespread freshening, which penetrates in the ocean interior along the same subduction pathways as the mean shallow salinity minimum from the eastern North Pacific. The freshening reaches the equator via the North Equatorial Current and counter currents, enhancing the already strong salinity front in the EUC. The North Pacific thermocline freshening is also seen to clearly penetrate through the Indonesian Seas to form a freshening plume extending to the eastern tropical Indian Ocean along the ITF tracer tongue (Fig. 10b), a pathway from the eastern Pacific to the equatorial Indian Ocean described by Gordon and Fine (1996).

In the South Pacific subtropical gyre, a more complex set of changes is evident. Two contrasting tongues of salinity changes are subducted west and equatorward—increased salinity to the east and freshened waters from the central basin outcrop. Both signals are driven largely by isopycnal migration (circles in Fig. 10b). In the south Indian Ocean, as for the upper thermocline, increased salinity is apparent basinwide on this surface, driven by surface salinity changes at the outcrop (diamonds in Fig. 10b), except where the ITF plume exists. In the north Indian Ocean, increased salinity is observed where the RSW (Beal et al. 2000) and PGW (Prasad et al. 2001) outflows are active.

c. *Mode waters* $\gamma^a = 26.75$ kg m^{-3}

SAMW are widespread in the Southern Hemisphere oceans and are characterized by the density range $\gamma^a =$ 26–27 kg m^{-3} (Hanawa and Talley 2001; Talley 2003). These waters outcrop between 40° and 50°S from where they are subducted equatorward and are generally found between 400 and 500 dbar in the subtropical ocean interior (Figs. 10c,7b,e,h).

In this important water mass, a global Southern Hemisphere isopycnal freshening is found, particularly for the Atlantic and Indian Oceans (Fig. 10c). Larger-magnitude changes are found closer to the outcrops in the South Atlantic and Indian Oceans. In the near-equatorial regions, which are ventilated on longer time scales, salinity changes are much weaker (Fig. 10c). The magnitude of the changes corresponds closely with CFC-11 concentrations (Figs. 7c,i) and also explains the more pervasive larger basinwide freshening signal in the lower-latitude Indian Ocean subtropics compared to the Atlantic (Fig. 10c). The broad-scale, basinwide freshening signature indicates that subtropical Indian Mode Waters have ventilated during the 50-yr analysis period, a conclusion supported by Fine et al. (2008). The comparative deeper, stronger ventilation (cf. depth of 200 pmol kg^{-3} contour, Figs. 7c,i) drives the broader basinwide changes. This broad-scale SAMW freshening is consistent again with the analysis at the outcrops, where freshening is due to isopycnal migration (circles in Fig. 10c), a southward migration of the ACC front (Alory et al. 2007).

The South Pacific shows a large contrast from west to east in the basin. In the west Pacific east of New Zealand at 168°W, a constrained freshening is apparent at the outcrop following the western Pacific subduction pathway described by Sallée et al. (2010). This change is partly F_W and partly migration driven, extending north and westward into the subtropics. In the eastern basin, weak changes from both sources are apparent, with only a small-amplitude freshening observed along the subtropical gyre subduction pathway.

In the North Atlantic, a less spatially coherent and weak freshening is found in the subtropical gyre, again corresponding with the surface analysis, which shows that poleward migration drives freshening at the outcrops (circles in Fig. 10c). In the North Pacific, a broad and coherent freshening is apparent in the Subtropical Mode Water (STMW) pool south and east of Japan (Fig. 10c). In the subpolar gyre and eastern subtropical gyre, increased salinities are found that are stronger and more widespread on the denser surfaces beneath.

Increased salinity is found at $\gamma^a = 26.75$ kg m^{-3} in the Arabian Sea, as discussed earlier, with the largest changes found near the outflows of the Red Sea and Persian Gulf, strongly suggesting that they are the source of this salinity change (Fig. 10c). On this surface the very high-salinity PGW is likely a more dominant contributor compared to RSW (Prasad et al. 2001). Negligible salinity change is found in the Bay of Bengal (Fig. 10c), which is poorly ventilated on this surface.

In summary, most mode waters around the global are freshening and this is largely due to warming-driven outcrop migration (circles in Fig. 10c). Change in magnitudes are considerably smaller than those found in the thermocline, an expected result given the longer ventilation time scales and larger volumes of mode waters.

d. *Deep waters* $\gamma^a = 27.5$ kg m^{-3}

Much like intermediate waters, the $\gamma^a = 27.5$ kg m^{-3} isopycnal outcrops between 50° and 60°S and near 70°N in the high-latitude North Atlantic and is found at depths of around 1200 dbar in the ocean interior for most of the globe (Figs. 10d,7b,e,h). Because of its

outcropping in the subpolar regions, this surface does not undergo active subduction but instead is subject to Ekman suction (Tomczak and Godfrey 1994). Compared to surfaces examined earlier, a clear reduction in the diagnosed salinity change is found, consistent with the slow ventilation of these waters.

Coherent patterns of change are observed on this surface—increased salinity centered at 55°S, just north of the surface outcrop, which is circumpolar in extent (Fig. 10d). The simplest explanation for this circumpolar change is a southward shift of the ACC core, as described by the analyses of historical temperature data (Gille 2002; Alory et al. 2007).

A broad salinity increase in the Atlantic basin between 50°S and 20°N is observed, also described by Curry et al. (2003). Increasingly, saline MOW could drive such a change; however, a clear intensification of the Atlantic change near the MOW plume over the period 1950–2008 is not observed (Fig. 10d). Below this level, a freshening of the Labrador Seawater (LSW) is evident along the $\gamma^a = 27.8$ kg m^{-3} surface (Figs. 9a and 7a,c), with magnitude, sign, and spatial extent agreeing well with Curry et al. (2003; their Fig. 1B). A similar freshening associated with the Greenland Iceland and Norwegian (GIN) Seas is also found, consistent with Curry and Mauritzen (2005) and Boyer et al. (2007).

10. Discussion and summary

Robust multidecadal linear trends to global ocean salinity patterns have been described for the period 1950–2008. These appear organized around the structure of global ocean–mean surface salinity, surface forcing patterns, and ocean ventilation pathways. Through exploiting the Argo observations, which provide unprecedented global data coverage, and attempting to carefully reduce eddy, seasonal, spatial, and interannual aliasing errors, the resolved change fields are more coherent and interpretable than previous studies and provide consistent three-dimensional fields of change for all ocean-state variables.

There is clearly a low signal-to-noise ratio between the multidecadal changes and the dominant synoptic and eddy noise apparent in time-snapshot ocean profile data (Fig. 3). However, the common, coherent, and spatially broad-scale patterns of salinity change, which are found independently in all the major ocean gyres, provide compelling evidence that the reported changes are real. These coherent patterns could not possibly arise from statistical noise. Additional validation by a bootstrap error analysis provides further confidence in the resolved spatial patterns.

As previously indicated, it is crucial to recognize that subsurface salinity changes on pressure surfaces are a mixture of changes affected by both wind-driven heave and actual water-mass changes (perturbations to the *T*–*S* relationship). In most parts of the global ocean, both mechanisms drive salinity changes on pressure surfaces. For example, in the strongly warming tropical and subtropical Atlantic Ocean, deepening isopycnals drive strong salinity increases on pressure surfaces above 500 dbar (Fig. 7b).

By analyzing water-mass changes on an isopycnal, a clear kinematic link is evident between most subsurface isopycnal salinity changes and the combined effect of ocean ventilation and surface warming. In subtropical gyres in all ocean basins, increasing salinities are found on isopycnals, which outcrop equatorward of the surface salinity maxima and freshening on those that outcrop poleward of the surface salinity maxima—a phenomenon that to first order is likely a result of the subduction of a broad-scale and widespread surface warming observed over the last 50 yr (Solomon et al. 2007). In the upper ocean, 50 yr has been long enough for changes at poleward-migrating outcrops to be advected throughout the ventilated gyres. In the case of the ITF, these changes have even penetrated from the North Pacific into the south Indian Ocean through the Indonesian Seas.

It is likely that over the 1950–2008 period ocean circulation has experienced changes (e.g., Gille 2002; Alory et al. 2007); however, for most of the subsurface water-mass changes observed, circulation shifts are less important than the subduction of a ~0.5°C broad-scale global ocean surface warming (Solomon et al. 2007) by the climatological-mean circulation. This broad-scale warming drives the clear and repeating pattern of subduction-driven changes to subsurface salinity. As expected, exceptions exist, such as the salinity changes due to the southward shift of the ACC (Gille 2002; Alory et al. 2007) and the unexplained changes in the poorly ventilated subpolar gyre of the North Pacific.

The conclusion that most of the subsurface salinity changes diagnosed on isopycnals result from warming-driven isopycnal migration through the *mean* salinity field invalidates using these changes alone to deduce surface flux trends. The studies of Curry et al. (2003), Helm (2008), and Wong et al. (1999) use isopycnally averaged subsurface fields to argue that changes are attributable only to enhanced precipitation or evaporation at the outcrops, whereas warming alone can produce much of the observed changes through outcrop migration. However, at the ocean surface, a striking similarity between the salinity trends and the mean salinity pattern is found, reinforcing the perception that

the global hydrological cycle has already been significantly enhanced over the last 50 yr (Helm 2008; Hosoda et al. 2009; Solomon et al. 2007; Roemmich and Gilson 2009), with climate zone and interbasin contrasts significantly enhanced. Such changes are expected as a consequence of anthropogenic global warming (Solomon et al. 2007), with observed changes in the North Atlantic basin (20°–50°N, and 40 yr to 2006) already attributed to anthropogenic interference (Stott et al. 2008). In addition, the subsurface water-mass changes diagnosed are an independent confirmation of persistent and broad-scale ocean warming.

Comparisons of these results to previous studies are compiled in Table 1. There is a general agreement in the magnitude and sign among all studies, except in the regional seas around Antarctica and the far North Atlantic. In particular, a very long continuous time series extending from 1944 to 2008 (Hill et al. 2008), situated off the east coast of Tasmania, Australia, shows very good agreement with this study (+0.15 compared to $+0.165 \pm 0.06$). Another study, which largely uses independent data, undertaken in the equatorial Pacific (Cravatte et al. 2009) resolves similar spatial patterns of surface salinity change for the Pacific warm-pool region and reports surface density changes that agree within the error estimates resolved in the present study (-0.5 kg m^{-3} compared to -0.54 ± 0.089 kg m^{-3}).

Data sparsity, both temporal and spatial, remains a significant limitation to analyses of multidecadal changes in the ocean. For this study, the overwhelming dominance of data from the Argo Program could potentially bias the 50-yr trends toward the more recent period. The rate of global surface temperature increases underwent a step change in the early to mid-1970s (Levinson and Lawrimore 2008; Trenberth et al. 2007), which may be mirrored in ocean salinity changes. To check for this, an analysis on data from the period 1975–2008 was performed and found the resulting trends to be slightly larger than for the full 1950–2008 analysis, with similar though not identical spatial patterns. This result tends to support the idea that the rate of observed changes has increased in the latter half of the 20th century, and that these diagnosed 50-yr trends are not pathologically biased by the dominance of data from the Argo period.

A valuable extension to this study would be an examination of changes in the amplitude and phase of the seasonal cycle over 1950–2008. Such an extension would aim to attribute the reported linear salinity changes to a more specific process (such as a changing seasonal cycle), extending upon the 50-yr salinity changes described. Cravatte et al. (2009) and Delcroix et al. (2007) have already described an amplitude increase of the seasonal cycle in the equatorial Pacific.

A more quantitative understanding of the relative importance of 50-yr circulation or surface salinity changes in driving subsurface water-mass change is not currently possible using historical observations (because of incomplete global coverage both in time and space scales)—ocean salinity advective and diffusive convergences (let alone their 50-yr change) are simply too poorly known. Dedicated ocean-modeling experiments (with appropriate archiving of eddy bolus fluxes) are required to progress a quantified attribution and decomposition of the causes of reported salinity changes.

The salinity changes reported in this study are large and have a significant impact on the ocean stratification and density structure (to be described elsewhere) and thus will eventually influence the ocean circulation itself, especially at high latitudes where salinity is the dynamically active variable. Thus, besides being a marker of changes in the global hydrological cycle, salinity-driven impacts of ocean sequestration of heat and carbon need to be examined in the context of better projections of future climate change.

This analysis provides a globally consistent and stringent target for coupled climate modeling systems that are being developed and utilized for projections of future climate. Salinity changes not only help to constrain the poorly known intensification of the hydrological cycle, but they will also be sensitive to model parameterizations of ocean mixing and water-mass formation—key processes that affect the sequestration of carbon and heat.

Acknowledgments. This paper is a contribution to the Australian Climate Change Research Program and Commonwealth Scientific Industrial Research Organization (CSIRO) Wealth from Oceans Flagship. P.J.D. is supported by a joint CSIRO–University of Tasmania Ph.D. scholarship in Quantitative Marine Science (QMS). We acknowledge the sources of observed data utilized in this study: Taiyo Kobayashi, Toshio Suga, and Shinya Minato (JAMSTEC-IORGC) for the SeHyD and IOHB data, Ruth Curry and Alison MacDonald (WHOI) for the Hydrobase2 data, and Alejandro Orsi and Thomas Whitworth (Texas A&M University) for the SODB data. The Argo data were collected and made freely available by the International Argo Program and the national programs that contribute to it. (available online at http://www.argo.ucsd.edu and http://argo.jcommops.org). The Australian component of Argo is part of Australia's Integrated Marine Observing System (IMOS; available online at http://www.imos.org.au). Many thanks to the folks at the NODC—without their efforts to locate, obtain, and digitize high-quality historical ocean data, studies such as this would not be possible. In particular,

the sustained progress of the Global Oceanographic Data Archaeology and Rescue (GODAR; available online at http://www.nodc.noaa.gov/General/NODC-dataexch/NODC-godar.html) project must be acknowledged, we hope data discovery and recovery work will continue into the future. The authors would also like to thank numerous colleagues from CSIRO, CAWCR, and the University of Tasmania for valuable feedback and input into this project. The Centre for Australian Weather and Climate Research is a partnership between CSIRO and the Australian Bureau of Meteorology. The authors thank Drs. Trevor McDougall and Bernadette Sloyan of CSIRO, Julia Durack, Moya Durack, and three anonymous reviewers for helpful comments with early drafts of this manuscript. The authors declare that they have no competing financial interests. P.J.D. completed the analysis and shared responsibility for writing the manuscript. S.E.W. assisted in analysis and shared responsibility for writing the manuscript.

REFERENCES

Alory, G. S. W., S. Wijffels, and G. Meyers, 2007: Observed temperature trends in the Indian Ocean over 1960–1999 and associated mechanisms. *Geophys. Res. Lett.,* **34,** L02606, doi:10.1029/2006GL028044.

Antonov, J. I., S. Levitus, and T. P. Boyer, 2002: Steric sea level variations during 1957–1994: Importance of salinity. *J. Geophys. Res.,* **107,** 8013, doi:10.1029/2001JC000964.

Aoki, S., N. L. Bindoff, and J. A. Church, 2005: Interdecadal water-mass changes in the Southern Ocean between 30°S and 160°S. *Geophys. Res. Lett.,* **32,** L07607, doi:10.1029/2004GL022220.

Beal, L. M., A. Ffield, and A. L. Gordon, 2000: Spreading of Red Sea overflow waters in the Indian Ocean. *J. Geophys. Res.,* **105,** 8549–8564.

Belkin, I. M., S. Levitus, J. Antonov, and S. Malmberg, 1998: ''Great salinity anomalies'' in the North Atlantic. *Prog. Oceanogr.,* **41,** 1–68.

Bethoux, J., B. Gentilli, and D. Tailliez, 1998: Warming and freshwater budget change in the Mediterranean since the 1940s, their possible relation to the greenhouse effect. *Geophys. Res. Lett.,* **25,** 1023–1026.

Bindoff, N. L., and T. J. McDougall, 1994: Diagnosing climate change and ocean ventilation using hydrographic data. *J. Phys. Oceanogr.,* **24,** 1137–1152.

——, and ——, 2000: Decadal changes along an Indian Ocean section at 32°S and their interpretation. *J. Phys. Oceanogr.,* **30,** 1207–1222.

——, and Coauthors, 2007: Observations: Oceanic climate change and sea level. *Climate Change 2007: The Physical Science Basis,* S. Solomon et al., Eds., Cambridge University Press, 385–432.

Boyer, T. P., S. Levitus, J. Antonov, R. Locarnini, and H. Garcia, 2005: Linear trends in salinity for the World Ocean, 1955–1998. *Geophys. Res. Lett.,* **32,** L01604, doi:10.1029/2004GL021791.

——, ——, ——, ——, A. Mishonov, H. Garcia, and S. A. Josey, 2007: Changes in freshwater content in the North Atlantic Ocean 1955–2006. *Geophys. Res. Lett.,* **34,** L16603, doi:10.1029/2007GL030126.

Bryden, H. L., E. L. McDonagh, and B. A. King, 2003: Changes in ocean water mass properties: Oscillations or trends? *Science,* **300,** 2086–2088.

Bullister, J. L., 1989: Chlorofluorocarbons as time-dependent tracers in the ocean. *Oceanography,* **2,** 12–17.

Candela, J., 2001: Mediterranean water and global circulation. *Ocean Circulation and Climate—Observing and Modelling the Global Ocean,* G. Siedler et al., Eds., International Geophysics Series, Vol. 77, Academic Press, 419–429.

Cravatte, S., T. Delcoix, D. Zhang, M. McPhaden, and J. LeLoup, 2009: Observed freshening and warming of the western Pacific warm pool. *Climate Dyn.,* **33,** 565–589.

Curry, R., cited 2002: Hydrobase2: A database of hydrographic profiles and tools for climatological analysis. Woods Hole Oceanographic Institute. [Available online at http://www.whoi.com/science/PO/hydrobase/.]

——, and C. Mauritzen, 2005: Dilution of the northern North Atlantic Ocean in recent decades. *Science,* **308,** 1772–1774.

——, B. Dickson, and I. Yashayaev, 2003: A change in the freshwater balance of the Atlantic Ocean over the past four decades. *Nature,* **426,** 826–829.

Delcroix, T., S. Cravatte, and M. J. McPhaden, 2007: Decadal variations and trends in tropical Pacific sea surface salinity since 1970. *J. Geophys. Res.,* **112,** C03012, doi:10.1029/2006JC003801.

Dickson, R. R., J. Meincke, S. Malmberg, and A. J. Lee, 1988: The ''great salinity anomaly'' in the northern North Atlantic 1968–1982. *Prog. Oceanogr.,* **20,** 103–151.

Emori, S., and S. J. Brown, 2005: Dynamic and thermodynamic changes in mean and extreme precipitation under changed climate. *Geophys. Res. Lett.,* **32,** L17706, doi:10.1029/2005GL023272.

Fine, R. A., W. M. Smethie, J. L. Bullister, M. Rhein, D. Min, M. J. Warner, A. Poisson, and R. F. Weiss, 2008: Decadal ventilation and mixing of Indian Ocean waters. *Deep-Sea Res. I,* **55,** 20–37.

Gille, S. T., 2002: Warming of the Southern Ocean since the 1950's. *Science,* **295,** 1275–1277.

Giorgi, F., and P. Lionello, 2008: Climate change projections for the Mediterranean region. *Global Planet. Change,* **63,** 90–104.

Gordon, A. L., and R. A. Fine, 1996: Pathways of water between the Pacific and Indian oceans in the Indonesian seas. *Nature,* **379,** 146–149.

Gould, J., and Coauthors, 2004: Argo profiling floats bring new era of in situ ocean observations. *Eos, Trans. Amer. Geophys. Union,* **85,** 19, doi:10.1029/2004EO190002.

Grodsky, S. A., J. A. Carton, and F. M. Bingham, 2006: Low-frequency variation of sea surface salinity in the tropical Atlantic. *Geophys. Res. Lett.,* **33,** L14604, doi:10.1029/2006GL026426.

Hanawa, K., and L. D. Talley, 2001: Mode waters. *Ocean Circulation and Climate—Observing and Modelling the Global Ocean,* G. Siedler et al., Eds., International Geophysics Series, Vol. 77, Academic Press, 373–386.

Harrison, D. E., and M. Carson, 2007: Is the World Ocean warming? Upper-ocean temperature trends: 1950–2000. *J. Phys. Oceanogr.,* **37,** 174–187.

Held, I. M., and B. J. Soden, 2006: Robust responses of the hydrological cycle to global warming. *J. Climate,* **19,** 5686–5699.

Helm, K. P., 2008: Decadal ocean water-mass changes: Global observations and interpretation. Ph.D. thesis, University of Tasmania, 177 pp.

Hill, K. L., S. R. Rintoul, R. Coleman, and K. R. Ridgway, 2008: Wind-forced low-frequency variability in the East Australia

Current. *Geophys. Res. Lett.,* **35,** L08602, doi:10.1029/2007GL032912.

Holland, P. W., and R. E. Welsch, 1977: Robust regression using iteratively reweighted least squares. *Comm. Stat. Theory Methods,* **A6,** 813–827.

Hosoda, S., T. Sugo, N. Shikama, and K. Mizuno, 2009: Global surface layer salinity change detected by Argo and its implication for hydrological cycle intensification. *J. Oceanogr.,* **65,** 579–586.

Jacobs, S. S., C. F. Giulivi, and P. A. Mele, 2002: Freshening of the Ross Sea during the late 20th century. *Science,* **297,** 386–389.

Johnson, G. C., and A. H. Orsi, 1997: Southwest Pacific Ocean water-mass changes between 1968/69 and 1990/91. *J. Climate,* **10,** 306–316.

Josey, S. A., E. C. Kent, and P. K. Taylor, 1998: The Southampton Oceanography Centre (SOC) ocean–atmosphere heat, momentum, and freshwater flux atlas. Southampton Oceanography Centre Rep. 6, 30 pp. [Available online at http://www.noc.soton.ac.uk/ooc/REFERENCES/PREPRINTS/SOC_flux_atlas.pdf.]

Joyce, T. M., and J. Dunworth-Baker, 2003: Long-term hydrographic variability in the northwest Pacific Ocean. *Geophys. Res. Lett.,* **30,** 1043, doi:10.1029/2002GL015225.

Kobayashi, T., and S. Minato, cited 2005: The Pacific Ocean reference dataset: SeHyD. *First Argo DMQC Workshop,* La Jolla, CA, Scripps Institution of Oceanography. [Available online at http://www.jamstec.go.jp/ARGORC/documents/Pacific_dataset_SeHyD.pdf.]

——, and T. Suga, 2006: The Indian Ocean Hydrobase: A high-quality climatological dataset for the Indian Ocean. *Prog. Oceanogr.,* **68,** 75–114, doi:10.1016/j.pocean.2005.07.001.

Kouketsu, S., M. Fukasawa, I. Kaneko, T. Kawano, H. Uchida, T. Doi, M. Aoyama, and K. Murakami, 2009: Changes in water properties and transports along 24°N in the North Pacific between 1985 and 2005. *J. Geophys. Res.,* **114,** C01008, doi:10.1029/2008JC004778.

Lascaratos, A., W. Roether, K. Nittis, and B. Klein, 1999: Recent changes in deep water formation and spreading in the eastern Mediterranean Sea: A review. *Prog. Oceanogr.,* **44,** 5–36.

Levinson, D. H., and J. H. Lawrimore, 2008: State of the climate in 2007. *Bull. Amer. Meteor. Soc.,* **89,** S1–S179.

Luyten, J. R., J. Pedlosky, and H. Stommel, 1983: The ventilated thermocline. *J. Phys. Oceanogr.,* **13,** 292–309.

McDougall, T. J., 1987: Neutral surfaces. *J. Phys. Oceanogr.,* **17,** 1950–1964.

——, and D. R. Jackett, 2005: The material derivative of neutral density. *J. Mar. Res.,* **63,** 159–185, doi:10.1357/0022240053693734.

Meehl, G. A., and Coauthors, 2007: Global climate projections. *Climate Change 2007: The Physical Science Basis,* S. Solomon et al., Eds., Cambridge University Press, 747–845.

Orsi, A. H., and T. Whitworth, cited 2010: *Southern Ocean*. Vol. 1, *Hydrographic Atlas of the World Ocean Circulation Experiment (WOCE),* Texas A&M University. [Available online at http://wocesoatlas.tamu.edu/.]

Prasad, T. G., M. Ikeda, and S. P. Kumar, 2001: Seasonal spreading of the Persian Gulf water mass in the Arabian Sea. *J. Geophys. Res.,* **106,** 17 059–17 071.

Ridgway, K. R., J. R. Dunn, and J. L. Wilkin, 2002: Ocean interpolation by four-dimensional weighted least squares – Application to waters around Australasia. *J. Atmos. Oceanic Technol.,* **19,** 1357–1375.

Roemmich, D., and J. Gilson, 2009: The 2004–2008 mean and annual cycle of temperature, salinity, and steric height in the global ocean from the Argo Program. *Prog. Oceanogr.,* **82,** 81–100.

Roether, W., B. B. Manca, B. Klein, D. Bregant, D. Georgopoulos, V. Beitzel, V. Kovacevic, and A. Luchetta, 1996: Recent changes in eastern Mediterranean deep waters. *Science,* **271,** 333–335.

Rohling, E. J., and H. L. Bryden, 1992: Man-induced salinity and temperature increases in western Mediterranean deep water. *J. Geophys. Res.,* **97,** 191–198.

Sallée, J. B., K. Speer, S. R. Rintoul, and S. Wijffels, 2010: Southern Ocean thermocline ventilation. *J. Phys. Oceanogr.,* **40,** 509–529.

Sanchez-Gomez, E., S. Somot, and A. Mariotti, 2009: Future changes in the Mediterranean water budget projected by an ensemble of regional climate models. *Geophys. Res. Lett.,* **36,** L21401, doi:10.1029/2009GL040120.

Schmitt, R. W., 1995: The ocean component of the global water cycle: U.S. national report to the International Union of Geodesy and Geophysics, 1991–1994. *Rev. Geophys.,* **33** (Suppl.), 1395–1409.

Solomon, S., D. Qin, M. Manning, M. Marquis, K. Averyt, M. M. B. Tignor, H. L. Miller Jr., and Z. Chen, Eds., 2007: *Climate Change 2007: The Physical Science Basis*. Cambridge University Press, 996 pp.

Stott, P. A., R. T. Sutton, and D. M. Smith, 2008: Detection and attribution of Atlantic salinity changes. *Geophys. Res. Lett.,* **35,** L21702, doi:10.1029/2008GL035874.

Talley, L., 2003: Shallow, intermediate, and deep overturning components of the global heat budget. *J. Phys. Oceanogr.,* **33,** 530–560.

Tomczak, M., and J. S. Godfrey, 1994: *Regional Oceanography: An Introduction*. Pergamon Press, 422 pp.

Trenberth, K. E., 1984: Signal versus noise in the Southern Oscillation. *Mon. Wea. Rev.,* **112,** 326–332.

——, and Coauthors, 2007: Observations: Surface and atmospheric climate change. *Climate Change 2007: The Physical Science Basis,* S. Solomon et al., Eds., Cambridge University Press, 235–336.

Tsuchiya, M., 1968: Upper waters of the intertropical Pacific Ocean. *The Johns Hopkins Oceanographic Studies,* No. 4, The John Hopkins Press, 50 pp.

Wong, A. P. S., N. L. Bindoff, and J. A. Church, 1999: Large-scale freshening of intermediate waters in the Pacific and Indian oceans. *Nature,* **400,** 440–443.

——, ——, and ——, 2001: Freshwater and heat changes in the North and South Pacific Oceans between the 1960s and 1985–94. *J. Climate,* **14,** 1613–1633.